Wavefront Reconstruction of Subsurface Radar Imagery Acquired along Cylindrical Scan Trajectories.

by

Daniel Flores-Tapia

A Thesis submitted to the Faculty of Graduate Studies of

The University of Manitoba

in partial fulfilment of the requirements of the degree of

DOCTOR OF PHILOSOPHY

Department of Electrical and Computer Engineering

University of Manitoba

Winnipeg

THE UNIVERSITY OF MANITOBA

FACULTY OF GRADUATE STUDIES

*****

COPYRIGHT PERMISSION

Wavefront Reconstruction of Subsurface Radar Imagery
Acquired Along Cylindrical Scan Trajectories

BY

Daniel Flores-Tapia

A Thesis/Practicum submitted to the Faculty of Graduate Studies of The University of

Manitoba in partial fulfillment of the requirement of the degree

Of

Doctor of Philosophy

ABSTRACT

In recent years, the use radar technology has been proposed in a wide range of subsurface imaging applications. In most subsurface radar applications, the data acquisition process is performed along a linear scan trajectory. However, a growing number of novel applications, such as breast microwave imaging and wood inspection, require the use of non-linear scan trajectories in order to adjust to the geometry of the scan area. However, data sets collected along cylindrical scan trajectories present also the same problems existing in linearly scanned data. The most noticeable of these issues is the formation of non-linear target signatures. This phenomenon makes it difficult to properly assess of the dimensions and locations of the targets present in the scan area. In order to visualize the collected data, a reconstruction process must be performed. In this thesis, two novel reconstruction algorithms for subsurface radar data acquired along 2D and 3D cylindrical scan trajectories are proposed. These approaches process the spectrum of the collected data in order to locate the spatial origin of the target reflections and remove the spreading of the target signatures. Practical considerations, such as spatial resolution and sampling constraints are discussed and illustrated. The proposed algorithm was successfully tested using experimental data collected from phantoms that mimic high contrast subsurface radar scenarios. The reconstructed imagery was spatially accurate and within an execution time in the order of seconds. Furthermore, the recorded data sets were reconstructed using the confocal mapping approach, a state of the art cylindrical SR focusing technique[Confocal, ConExp]. The data sets reconstructed proposed technique exhibited a higher signal to noise ratios and better focus quality superior than the imagery focused using the confocal mapping approach.

ACKNOWLEDGMENTS

The author would like to greatly thank Dr. Gabriel Thomas for all his guidance, support and encouragement provided in the course of this research. The author would also like to thank Dr. Stephen Pistorius and Dr. Sima Noghanian for all the constructive criticism and suggestions that helped to greatly increase the quality of this thesis. I am also grateful to Mr. Zoran Trajkoski for all his help in the design and implementation of the data acquisition systems used in this project. Many thanks to Dr. Lotfolloah Shafai for all his suggestions regarding the use of radar absorbing material in the experimental setups. Last but no least, the author would like to remark the great help received by the technical staff at the department of Electrical and Computer engineering for supplying invaluable technical support provided during these last five years.

DEDICATION

To my wife, Karla, who I would like to thank for all her patience and support and to my son, Luis Guillermo, for the inspiration and motivation that he brought to my life.

And to my parents, Victor and Bertha, as the result of a promise made 22 years ago.

"Non nobis Domine"

TABLE OF CONTENTS

LIST OF TABLES

LIST OF FIGURES

LIST OF ACRONYMS

AB	Asymptotic Behavior.
IF	Instantaneous Frequency.
psf	point spread function.
SFCW	Stepped Frequency Continuous Wave.
SNR	Signal to Noise Ratio.
spf	spherical phase function
SR	Subsurface Radar.
UWB	Ultra Wide Band.

LIST OF SYMBOLS

a	Sample index in the discrete range domain.
b	Sample index in the discrete y cross-range domain.
B	Radiated signal bandwidth.
$D_p(\theta)$	Distance between the p^{th} scatter and the scan location positioned at (R,θ).
E_r	Dielectric permittivity.
f_c	Center frequency.
$f(t)$	Radiated waveform
$f(t^*)$	$f(t)$ evaluated at t^*.
$F(\omega)$	Fast-time spectrum of the radiated waveform.
$g(h(t))$	Auxiliary composite function.
$h(t)$	Auxiliary function phase term.
$i_p(x_a,y_b)$.	Rectangular spatial representation of the p^{th} target responses (circular scan trajectory).
$i_p(x_a,y_b,z_m)$	Rectangular spatial representation of the p^{th} target responses (cylindrical scan trajectory).
$I_p(k_{ux}, k_{uy})$	Rectangular spatial frequency spectrum from the reflection of the p^{th} target defined over the frequency points specified in (k_{ux},k_{uy}) (circular scan trajectory) .

$I_p(k'_x, k'_y, k'_z)$	Rectangular spatial frequency spectrum from the reflection of the p^{th} target (cylindrical scan trajectory).
$I_p(k'_{ux}, k'_{uy}, k'_z)$	Rectangular spatial frequency spectrum from the reflection of the p^{th} target defined over the frequency points specified in (k_{ux}, k_{uy}) (cylindrical scan trajectory).
$I_p(k'_x, k'_y)$	Rectangular spatial frequency spectrum from the reflection of the p^{th} target (circular scan trajectory).
$\mathrm{E}(k)$	Auxiliary spectral function.
k	Wavenumber.
k'	Discrete wavenumber.
$k_{er}(l', k'_z)$	Evenly spaced azimuth frequency plane.
k_m	Maximum wavenumber present in the radiated signal.
k_r	Radial spatial frequency domain.
$k_{ur}(\omega', k'_z)$	Auxiliary function for the azimuth spatial frequency remapping process.
k_{ux}	Uneven spaced location vector in the discrete x cross-range frequency domain.
k_{uy}	Uneven spaced location vector in the discrete cross-range frequency domain.
k'_x	Discrete x cross-range frequency domain.
k'_y	Discrete y cross-range frequency domain.
k_z	Azimuth spatial frequency domain.

k'_z	Azimuth discrete spatial frequency domain.
l	Sample index in the discrete time domain.
n	Sample index in the discrete angular domain.
m	Sample index in the discrete azimuth domain.
L	Total number of samples in the discrete time domain.
N	Total number of samples in the discrete angular domain.
M	Total number of samples in the discrete azimuth domain.
$L_p(\theta, z)$	Distance between the p^{th} scatter and the scan location positioned at (R, θ, z).
$psf_p(\Omega_{w,p}, w)$	Point spread function size of the p^{th} target responses along the w scan trajectory.
r_i	Scan area radius.
r_p	Radial location of the p^{th} target.
R	Radius of the scan geometry.
$s(t,\theta)$	Target responses collected at(R, θ).
$s_p(t,\theta)$	Collected responses from the p^{th} target collected at (R, θ).
$s(t_l,\theta_n)$	Sampled version of the target responses collected at (R, θ_n).
$s(t,\theta,z)$	Target responses collected at(R, θ, z).
$s(t_l,\theta_n,z_m)$	Sampled version of the collected target responses collected at (R, θ_n, z_m).
$S_p(\omega,\theta)$	Fast-time spectrum of the p^{th} target responses in a circular scan trajectory.

$S_p(\omega,\varepsilon)$	Slow-time spectrum of the p^{th} target responses in a circular scan trajectory.
$S(\omega',\varepsilon')$	Sampled version of the slow-time spectrum from the p^{th} target responses collected along a circular scan trajectory.
$S_p(\omega,\theta,z)$	Fast-time spectrum of the collected target responses in a cylindrical scan trajectory
$S_p(\omega,\varepsilon,k_z)$	Slow-time spectrum of the p^{th} target responses in a cylindrical scan trajectory.
$S(\omega',\varepsilon',k'_z)$	Sampled version of the slow-time spectrum from the p^{th} target responses collected along a cylindrical scan trajectory.
t	Time domain.
t^*	Stationary point in the time domain.
T	Total number of targets inside the scan area.
$sinc$	Sinc function
$SNR_{c,2D}$	Signal to Noise Ratio of the circular data focused using the confocal mapping approach.
$SNR_{c,3D}$	Signal to Noise Ratio of the cylindrical data focused using the confocal mapping approach.
$SNR_{w,2D}$	Signal to Noise Ratio of the circular data focused using the wavefront reconstruction approach.

$SNR_{w,3D}$	Signal to Noise Ratio of the cylindrical data focused using the wavefront reconstruction approach.
$U_p(\omega',\varepsilon')$	Matched filtered slow-time spectrum of the p^{th} target responses.
$U_p(k_r,\varepsilon',k'_z)$	Matched filtered-azimuth remapped, slow-time spectrum of the p^{th} target responses.
$U_p(k_r,\theta_n,k'_z)$	Matched filtered-azimuth remapped fast-time-azimuth spectrum of the p^{th} target responses.
$U_p(\omega',\varepsilon',k'_z)$	Matched filtered slow-time spectrum of the p^{th} target responses.
v_s	Lower limit of $\mathrm{E}(k)$ range.
v_f	Upper limit of $\mathrm{E}(k)$ range.
w	Generic slow-time domain
w	Stationary point in the w slow-time domain
W	Total number of data clusters in the image.
w_d	d^{th} data cluster in the image histogram.
x	x cross range domain.
x_p	x location of the p^{th} target.
y	y cross range domain.
y_p	y location of the p^{th} target.
z	Azimuth cross range domain.
z_i	Scan area azimuth length.
z_{min}	Lower azimuth coordinate of the scan geometry.
z_{max}	Upper azimuth coordinate of the scan geometry.

z_p	Azimuth location of the p^{th} target.
z^*	Stationary point in the azimuth domain.
α^*	Angle opposite to r_p (circular scan trajectory).
β^*	Angle opposite to R (circular scan trajectory).
α_z^*	Angle opposite to r_p (cylindrical scan trajectory).
β_z^*	Angle opposite to R (cylindrical scan trajectory).
$\chi(R', r', z')$	Auxiliary function used by $\Omega_{\theta,p}$.
$\gamma(\omega', \varepsilon')$	Components in the slow-time sampled spectrum related to the delays produced by the shape of the cylindrical scan aperture (cylindrical scan trajectory).
$\gamma(\omega', \varepsilon')^+, C(\omega', \varepsilon')$	Complex conjugate of $\gamma(\omega', \varepsilon', k'_z)$
$\gamma(\omega', \varepsilon', k'_z)$	Components in the slow-time sampled spectrum related to the delays produced by the shape of the cylindrical scan aperture (cylindrical scan trajectory).
$\gamma(\omega', \varepsilon', k'_z)^+, C(\omega', \varepsilon', k'_z)$	Complex conjugate of $\gamma(\omega', \varepsilon', k'_z)$.
$\delta\theta$	Sample spacing in the angular scan trajectory.
δz	Sample spacing in the azimuth scan trajectory.
Δf	Frequency increment.
Δk_r	Radial spatial frequency increment.
$\Delta k'_y$	Discrete y cross-range spatial frequency increment.
$\Delta k'_x$	Discrete range spatial frequency increment.

Δt_p	Range resolution.
$\Delta\theta(r_i, z_i)$	Angular resolution under ideal illumination conditions.
$\Delta\theta(\vartheta_\theta, \vartheta_z)$	Angular resolution under partial illumination conditions.
$\Delta z(r_i, z_i)$	Azimuth resolution under ideal illumination conditions.
$\Delta z(\vartheta_\theta, \vartheta_z)$	Azimuth resolution under partial illumination conditions.
ε	Angular spatial frequency domain.
ϕ_p	Angular location of the p^{th} target.
φ	Auxiliary term used to reduce the size of the angular resolution expressions.
$\Gamma_{p,3dB}^{2D}$	Magnitude of the 3dB point of the p^{th} target signature in the circular data focused using the wavefront reconstruction approach.
$\Gamma_{p,3dB}^{c,2D}$	Magnitude of the 3dB point of the p^{th} target signature in the circular data focused using the confocal mapping approach.
$\Gamma_{p,3dB}^{3D}$	Magnitude of the 3dB point of the p^{th} target signature in the cylindrical data focused using the wavefront reconstruction approach.
$\Gamma_{p,3dB}^{c,2D}$	Magnitude of the 3dB point of the p^{th} target signature in the cylindrical data focused using the confocal mapping approach.
ϑ	Antenna beamwidth size.
ϑ_θ	Antenna beamwidth size in the angular domain.
ϑ_z	Antenna beamwidth size in the azimuth domain.

$\kappa_p(\omega',\varepsilon')$	Components in the slow-time sampled spectrum related to the p^{th} target responses (circular scan trajectory).
$\kappa_p(\omega',\varepsilon',k'_z)$	Components in the slow-time sampled spectrum related related to the p^{th} target responses (cylindrical scan trajectory).
λ_c	Wavelength corresponding to the center frequency present in the radiated signal.
λ_m	Minimum wavelength present in the radiated signal.
λ	Generic slow-time domain.
λ^*	Stationary point in the λ slow-time domain.
$\mu(t)$	Generic phase modulating term.
$\mu(t^*)$	$\mu(t)$ evaluated at t^*.
$\mu(\lambda, w)$	Generic phase modulating term.
$\mu(\lambda, w)$	$\mu(\lambda, w)$ evaluated at (λ^*, w^*).
η	Random variable corresponding to the pixel intensity levels in the image.
ν	Medium propagation speed.
ρ	Auxiliary term used to reduce the size of the angular resolution expressions.
σ^c	Signal to Noise Ratio of the circular data focused using the confocal mapping approach.
σ^w	Standard deviation of the background noise in the data focused using the wavefront reconstruction approach.

θ	Angular domain.
θ_n	Discrete angular domain.
θ^*	Stationary point on the angular domain in a circular scan geometry.
θ_z^*	Stationary point on the angular domain in a cylindrical scan geometry.
ω	Temporal frequency domain
ω'	Discrete temporal frequency domain
ω_{min}	Minimum frequency present in the radiated waveform.
ω_{max}	Maximum frequency present in the radiated waveform.
ϖ_z	Angle between the antenna center and the target in the azimuth direction.
ϖ_θ	Angle between the antenna center and the target in the angular direction.
$\Psi_p(\omega,k_z)$	Spectrum amplitude component of $S_p(\omega,\theta,k_z)$.
$\zeta(\omega,\varepsilon)$	Amplitude component of $S(\omega,\varepsilon)$.
$U_p(\omega',\varepsilon')$	Amplitude component of $S(\omega',\varepsilon)$.
$\zeta_p(\omega,\varepsilon,k_z)$	Amplitude component of $S_p(\omega,\varepsilon,k_z)$.
$\zeta_p(\omega',\varepsilon',k'_z)$	Amplitude component of $S(\omega',\varepsilon',k'_z)$.
$\Omega_{\theta,p}$	Support band of the of the p^{th} target responses along the angular scan trajectory.

$\Omega_{z,p}$ Support band of the of the p^{th} target responses along the azimuth scan trajectory.

$|\Omega_{w,p}|$ Magnitude of the support band from the p^{th} target responses along the w scan trajectory.

1. INTRODUCTION

Subsurface radar overview

Subsurface Radar (SR) techniques have been extensively used in a wide variety of applications for non invasive inspection and imaging purposes, such as landmine detection, soil humidity estimation, archeology and wood inspection. Similarly to conventional radar, SR technology is used to determine the locations and sizes of foreign objects located within the scanned region. SR approaches are normally applied in scenarios that satisfy two conditions. First, the materials present in the scan area are a suitable medium for the propagation of electromagnetic waves. Secondly, the dielectric properties of those materials and the targets exhibit a noticeable contrast [1]. In general, SR system architectures can be described based on two features:

Waveform. Stepped Frequency Continuous Wave (SFCW) and pulse based patterns are the most commonly used Ultra Wide Band (UWB) waveforms for SR data acquisition. Pulse based systems irradiate a short duration (few nanoseconds) impulse-shaped waveform at a constant repetition rate. On the other hand, SFCW radar systems transmit a series of harmonics from a reference sine wave separated by Δf Hz [2]. Although most of the commercial SR systems are pulse based, SFCW SR systems are becoming popular due to their capabilities to mimic the spectrum of different waveforms and higher irradiation power.

Scan Geometry. The geometry of the scan trajectory is given by the shape of the area to be imaged [1]. Currently, the data acquisition process in most of the SR applications is done using either planar or cylindrical scan trajectories. In planar trajectories, the scan locations are positioned in a straight line along the surface of the area of interest. In this morphology, every scan location is facing downwards. Linear scan trajectories are usually used in geophysical SR applications, although some modified linear geometries are also used for breast cancer detection purposes [3, 4]. Cylindrical scan trajectories are defined on a circular aperture that encloses the scan area. In this configuration all the scan locations face towards the center of the circular aperture. This geometry is used in quite recent SR applications, such as breast microwave imaging and wood inspection [4, 5].

A diagram of these scan trajectories is shown in figure 1.1. It is important to indicate that these scan geometries are defined in a 2D plane. If a 3D model of the scan area is needed, a set of these trajectories is positioned at different locations along the azimuth axis of the scan area.

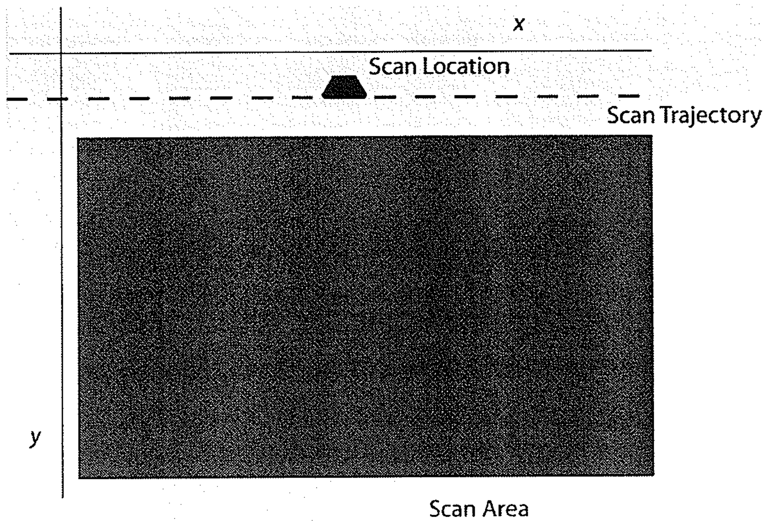

a)

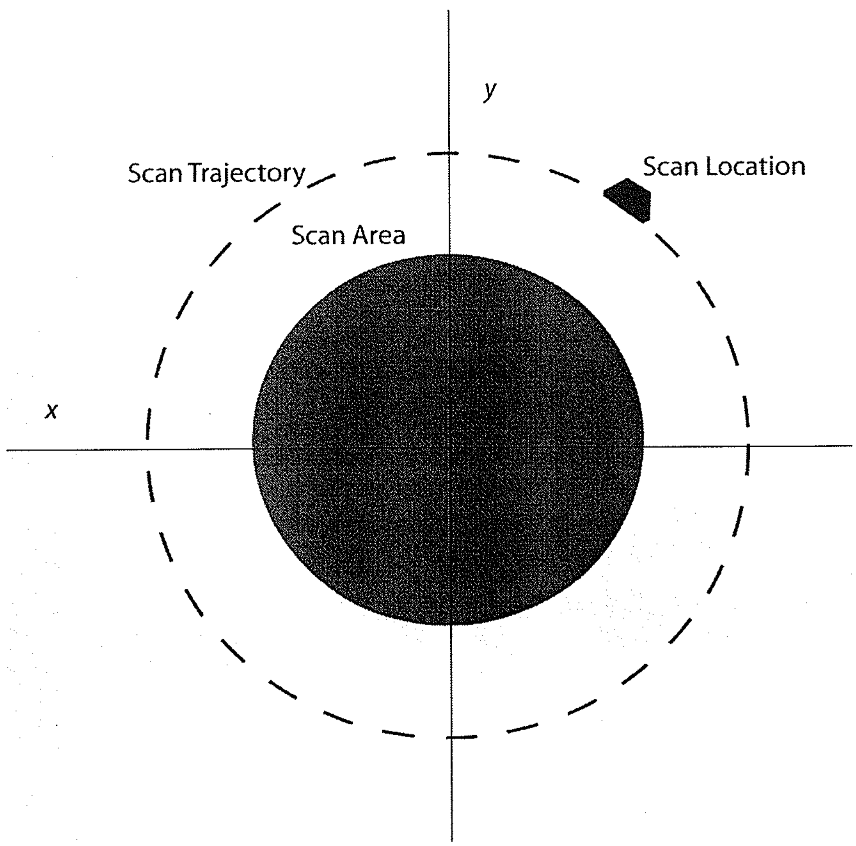

b)

Figure 1.1. a) Planar scan trajectory, b) Cylindrical scan trajectory.

In scenarios where the targets are located at near field distances, the standard SR data acquisition methodology is the following. First, a series of scan locations are defined such as they are positioned parallel to the surface of the scan area. Next, an UWB waveform is radiated at each scan location. Finally, the reflections from scattering objects inside the scan area are then recorded, processed and displayed in order to be interpreted. This process can be performed using one antenna per scan location or, if the number of available antennas is smaller than the number of scan locations, by irradiating at multiple scan locations with a movable antenna set. If this last option is chosen, the antennas are moved using discrete steps. The scan time at each location is determined by the data acquisition instrumentation.

Problem definition

As the irradiation is performed along the scan trajectory, the target responses will have different travel times, resulting in the formation of non-linear signatures [6, 7]. Target signatures present greater dimensions than the original inclusion sizes and in certain cases an overlap between different signatures may occur. These phenomena make the assessment of the actual dimensions and locations of the targets present in the scan area a difficult task. Some examples of this phenomenon are shown in figure 1.2. SR data must be focused to properly visualize the target responses [6, 7]. Due to the fact that targets in SR applications are located at distance that falls within the near-field of the antenna irradiation pattern, the use of conventional radar reconstruction techniques based on plane wave assumptions do not yield accurate results [8,9]. A considerable number of reconstruction approaches have been developed for SR data focusing purposes [10, 11, 12, 13, 14, 15]. In general, these methods can be classified as either time-shift techniques or wavefront reconstruction approaches [13]. Time-shift techniques perform a shift-sum process over a set of regions of interest in the scan area. The target responses are delayed according to the location where they were obtained and their distance from the regions of interest. Next, the shifted responses are added and the square of the sum is the energy at the region of interest. The same process is repeated for all the regions of interest in the scan area [16]. Two examples of this approach are the confocal mapping algorithm [10,17], the beamforming reconstruction approach [11, 18] and the time-reversal method [14, 19].

Contrary to time-shift techniques, wavefront reconstruction techniques focus the data by performing a series of operations in the frequency domain [20, 21]. The spectrum of the collected reflections, both in the signal travel time and the scan trajectory directions, is calculated. The phase of the recorded signals is modified in order to transfer the data from the domain where it is originally acquired to the spatial domain where it will be displayed. Finally, the Fourier transform of the compensated spectrum is computed in order to properly visualize the data [14]. Although each method has advantages and disadvantages of their own, time-shift techniques are characterized by their low computational cost, while wavefront reconstruction approaches exhibit a higher Signal to Noise Ratio (SNR) and an increased focus quality [13, 23].

Although the vast majority of these approaches are designed to focus SR data acquired along linear scan trajectories, some focusing techniques for cylindrical scan trajectories have been also developed [12, 18]. However, these approaches still have limitations, such as artifact formation and low Signal to Noise Ratio (SNR) values [23], which may lead to an inaccurate reconstruction of the collected data. Thus, the development of a robust reconstruction method for SR data acquired along cylindrical scan trajectories poses as a challenging problem.

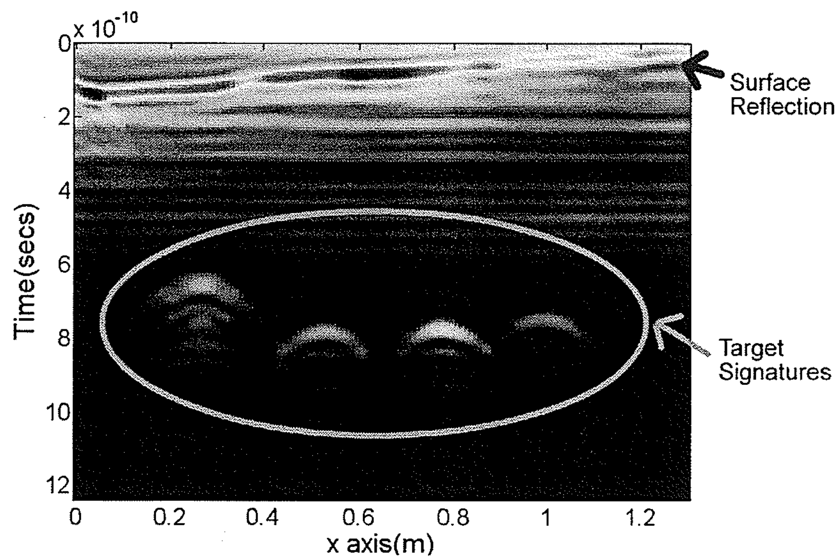

a)

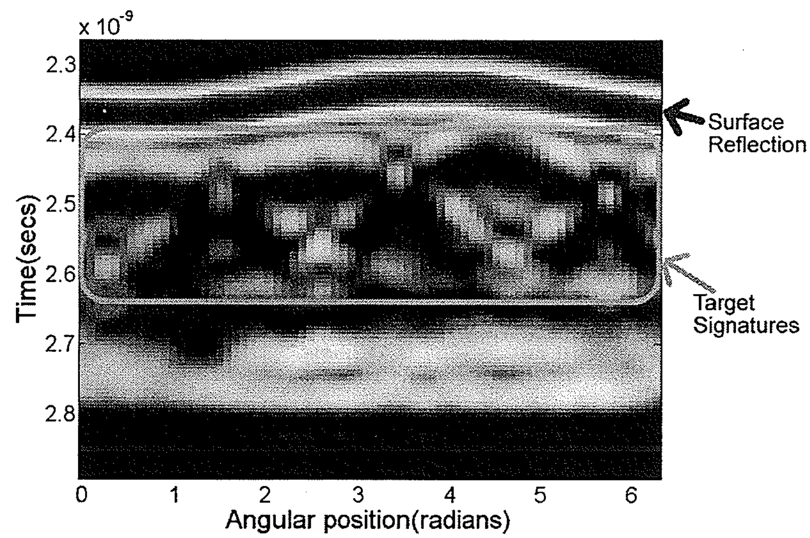

b)

Figure 1.2. Unproccesed experimental SR imagery corresponding to: a) 4 metal rods buried in sand, data acquired along a linear scan trajectory, b) 2 metal ovoids inside a pvc pipe, data acquired along a cylindrical scan trajectory.

1.3 Contribution

In this thesis, a wavefront reconstruction approach for SR data acquired along cylindrical scan trajectories is proposed. The proposed algorithm can be summarized as follows. First, the spectrum of the collected data is calculated along the signal travel time and scan trajectory directions. Next, the effects of the scan trajectory are removed using a matched filter. The compensated spectrum is then migrated from its original spatio-temporal frequency domain to a rectangular frequency space. Finally, in order to visualize the focused data in the spatial domain, the inverse Fourier transform of the migrated spectrum is calculated.

The proposed method was developed by analyzing the frequency response of the Green's function, also called spherical phase function (spf), of a generic cylindrical scan geometry [8, 24]. A closed expression for the spectrum of the spf was calculated using the stationary phase method [25]. The resulting expressions do not include any terms in the form of Hankel functions, making the proposed reconstruction method computationally efficient. Furthermore, the support bands of the spf spectrum were determined in order to determine the size of the point spread function (psf). The outcome of this analysis was a series of expressions that yield the spatial resolution and sampling constraints of the proposed approach. The mathematical derivations leading to the theoretical analysis of the spf were entirely done by the author.

The proposed reconstruction method was tested and validated using simulated and experimental data sets. In order to evaluate the performance of the proposed method with respect to current focusing approaches, the experimental data sets were reconstructed using the confocal mapping approach, a state of the art technique for SR data acquired along cylindrical scan trajectories [12, 17]. The images obtained by using the proposed technique presented more accurate target signatures and exhibited higher SNR values than the models generated by the confocal mapping approach. This thesis is organized as follows. In chapter 2, a wavefront reconstruction approach for 2D cylindrical (also known as circular) scan trajectories is explained. The extension of this reconstruction method into 3D cylindrical trajectories is described in chapter 3. Theoretical aspects of the proposed method, such as the nature of the point spread function, sampling constraints and spatial resolution, are described in chapter 4. In chapter 5, the performance of the proposed technique is assessed using simulated and experimental data. Finally, concluding remarks can be found in chapter 6.

2. WAVEFRONT RECONSTRUCTION OF CIRCULAR SR DATA.

2.1 Signal Model

Consider a circular aperture with a radius R defined in the (x,y) plane. As specified in the previous section, in this scan geometry each scan location is facing towards the center of the aperture. A total of T point scatters are assumed to be located inside the area delimited by the scan trajectory. In the following discussion, the center of the aperture will be considered the origin of the coordinate system. Also, a polar coordinate system will be used in order to simplify the calculations. Under these considerations, the location of the p^{th} scatter is (r_p, ϕ_p), where $r_p = \sqrt{x_p^2 + y_p^2}$ and $\phi_p = \tan^{-1}\left(\frac{y_p}{x_p}\right)$. The distance between the scan location at (R,θ) and the p^{th} scatterer is given by $D_p(\theta) = \sqrt{R^2 + r_p^2 - 2 \cdot R \cdot r_p \cos(\phi_p - \theta)}$. A diagram of this model is illustrated in figure 2.1.

A signal $f(t)$ is irradiated at each scan location and the received signal can be expressed as:

$$s(t,\theta) = \sum_{q=1}^{T} \sigma_q \cdot f\left(t - \frac{2\sqrt{R^2 + r_q^2 - 2 \cdot R \cdot r_q \cos(\phi_q - \theta)}}{v}\right), \text{ for } \theta \in [0, 2\pi] \tag{2.1}$$

where $s(t,\theta)$ are the collected responses from the scatters at the (t,θ) domain, v is the medium propagation speed and σ_q is the reflectivity of the q^{th} scatter [8], which is assumed to be a constant for now.

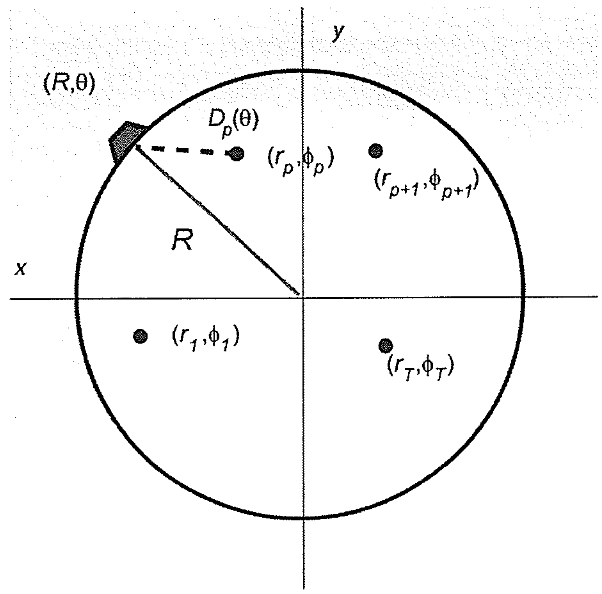

Figure 2.1. Circular scan trajectory geometry.

The collected data is a function of t and θ. Every radar signal model is a function of two types of scan trajectories [8]. The fast-time trajectory is present in every radar system and it corresponds to the signal travel time between the antenna and the target. The slow-time trajectories correspond to the switching time between the scan locations. The reason for this naming convention occurs because the elapsed time between adjacent locations along the fast-time direction is much less than between contiguous positions in the slow-time directions [8]. In a circular scan system, the fast-time trajectory is t, while the slow-time trajectory is θ.

2.2 Spherical phase function analysis

Target reflections present nonlinear signatures due to the different signal travel times along the slow time trajectory [1, 6, 8]. If the spectrum of the collected data is calculated along the fast time trajectory, it can be observed that instantaneous frequency of this spectrum decreases as we come closer to the spatial locations of the targets in the slow time trajectory [8, 18]. This phenomenon, also known as radar-doppler effect, can be used to migrate the collected target responses to their original spatial locations [8]. The methods that apply this methodology are known as wavefront reconstruction or holography approaches [8, 24]. Holography techniques have been successfully used to reconstruct SR data acquired along linear trajectories. This method is also known as Stolt's interpolation or F-K migration algorithm [3, 10, 26]. Nevertheless, as explained in [8] and [25], although most of the existing holography approaches share a similar methodology, the nature of each wavefront reconstruction approach is dictated by the shape of its scan geometry. This is because the features of the target reflection delays are different for each scan trajectory. These variations lead to differences in the behavior of the radar-doppler variations. In the following discussion, the theoretical basis for the wavefront reconstruction of data acquired along circular trajectories will be illustrated.

Let consider the response from the p^{th} scatterer:

$$s_p(t,\theta) = \sigma_p \cdot f(t - \frac{2D_p(\theta)}{v}). \tag{2.2}$$

By calculating the Fourier transform of (2.2) along the fast-time direction t, the following expression (also known as the spherical phase function of the system) is obtained:

$$S_p(\omega,\theta) = \sigma_p F(\omega) \cdot \exp(-i(2k \cdot D_p(\theta))), \qquad \text{for } k \in [\omega_{\min}/v, \omega_{\max}/v] \tag{2.3}$$

where $k = \frac{\omega}{v}$ is the wavenumber. As the responses from the p^{th} scatter are collected along the scan trajectory, a phase modulated signal can be observed also in the slow-time direction θ. The spectrum of such signal can be obtained by calculating the Fourier transform of (2.3) in the θ direction resulting in the following expression:

$$S_p(\omega,\varepsilon) = \int_0^{2\pi} \sigma_p F(\omega) \cdot e^{-i(2k \cdot D_p(\theta) + \varepsilon\theta)} d\theta, \tag{2.4}$$

where ε is the frequency counterpart of θ.

For large k values- such as is required by many UWB systems- the result of the integral in (2.4) rapidly approaches to zero [25]. This behavior is further described in the appendix I. However, it is possible to obtain an asymptotic function that describes how fast the exponential term approaches zero for large k values. As discussed in [25], this kind of integrals can be analytically solved by using the stationary phase method. This technique uses the behavior of the rate of change of the frequency, also known as Instantaneous Frequency (IF), of the angle function to determine the Asymptotic Behavior (AB) of the desired function. In general, the IF value of a function $g(h(t))$, where $h(t)$ is the phase term, is given by $\partial(h(t))/\partial t$. The AB of an integral of the form $\mathrm{E}(k) = \int_{v_s}^{v_f} f(t)\exp(j \cdot k \cdot \mu(t))dt$, is obtained by evaluating the spf at the value of the stationary point of the phase function $\mu(t)$, t^*, yielding, [25]:

$$E(k) = 2f(t^*)\exp(j \cdot k \cdot \mu(t^*)). \tag{2.5}$$

First, the IF value of the spf along the θ direction is determined as follows:

$$\frac{d(-2k \cdot D_p(\theta)-\varepsilon\theta)}{d\theta}=\frac{2k \cdot Rr_p \sin(\phi_p-\theta)}{\sqrt{R^2+r_p^2-2 \cdot Rr_p \cos(\phi_p-\theta)}}-\varepsilon \cdot \tag{2.6}$$

As discussed in [25], a stationary point θ^* is achieved when (2.6) equals zero. Therefore:

$$\left[-\frac{2k \cdot Rr_p \sin(\phi_p-\theta)}{\sqrt{R^2+r_p^2-2 \cdot Rr_p \cos(\phi_p-\theta)}}-\varepsilon\right]_{\theta=\theta^*}=0 \cdot \tag{2.7}$$

From (2.7) the following relationship can be obtained:

$$\frac{\sin(\phi_p-\theta^*)}{\sqrt{R^2+r_p^2-2 \cdot Rr_p \cos(\phi_p-\theta^*)}}=-\frac{\varepsilon}{2kRr_p} \cdot \tag{2.8}$$

A simple way of obtaining the value of θ^* is by treating (2.8) as a sine law relationship. As illustrated in figure 2.2, the considered scatter, the antenna and the center of the trajectory form a triangle. Therefore, from basic trigonometry it can be shown that $\theta^* = \phi_p + \alpha^* + \beta^* - \pi$, where α^* and β^* are the complimentary angles of θ^*. Given that the sine law applies for all the angles in the triangle, $\alpha^* = -\sin^{-1}(\varepsilon/2kR)$ and $\beta^* = -\sin^{-1}(\varepsilon/2kr_p)$. Substituting the value of θ^* in (2.4) yields:

$$S_p(\omega,\varepsilon)=\sigma_p\cdot\zeta(\omega,\varepsilon)\cdot\exp\left(-i(\sqrt{4k^2r_p^{\,2}-\varepsilon^2}+\sqrt{4k^2R^2-\varepsilon^2}+\varepsilon\cdot\sin^{-1}\left(\frac{\varepsilon}{2kR}\right)+\varepsilon\cdot\sin^{-1}\left(\frac{\varepsilon}{2kr_p}\right)+\varepsilon\pi-\varepsilon\phi_p)\right) \quad (2.9)$$

where $\zeta_p(\omega,\varepsilon)$ is the spectrum amplitude component in the (ω,ε) frequency space.

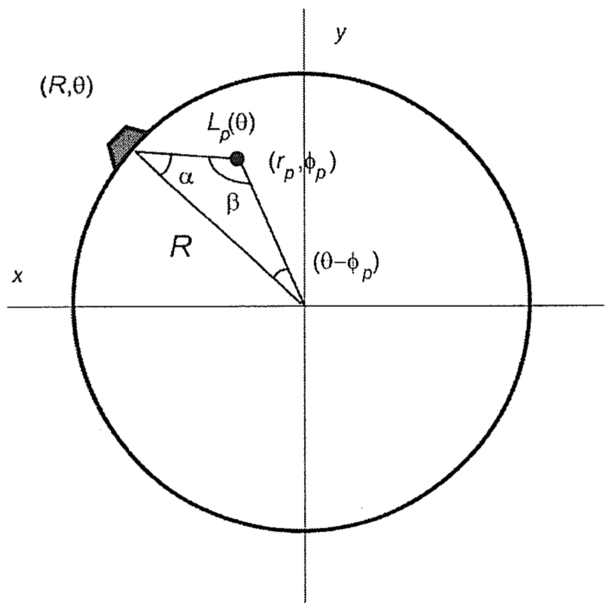

Figure 2.2. Angle geometry and nomenclature.

2.3 Image reconstruction

As mentioned in the previous discussion, the collected data is a function of the signal travel time between the antenna and the targets. As shown in figure 2.3, if the collected data is mapped directly to a rectangular coordinate system, the target signatures appear at shifted locations and present a considerable increase on their dimensions. In order to properly visualize the target responses, the measured data must be transferred from its original spatial temporal space to the spatial space related to the dimensions of the scan area.

In the vast majority of the SR applications, the data set $s(t,\theta)$ takes the form of an evenly sampled discrete space. This is due to the fact that most of the SR data is acquired and processed using digital equipment. The sampled version of $s(t,\theta)$, $s(t_l,\theta_n)$, is defined over a $L \times$ grid, where L is the number of time samples, N is the total scan locations in the circular scan aperture, and l, n denote the sample indexes along t and θ scan trajectories correspondingly. Provided that the sampling process satisfies the Nyquist-Shannon theorem [27], the theoretical analysis shown in the last subsection holds true for the 2D discrete Fourier transform of $s(t_l,\theta_n)$, defined as $S(\omega',\varepsilon')$, where ω' and ε' are the discrete counterparts of ω and ε respectively.

The first step is to compensate for the effects of the scan trajectory on the collected data. As shown in (2.9), the spectrum of the spf is formed by two main components [7, 28]. The first type, denoted as $\kappa_p(\omega',\varepsilon')$, are the PM terms related to the target responses. These terms are a function of the target location, (r_p,θ_p). The second type of spectral components, $\gamma(\omega',\varepsilon')$, are the PM terms related to the delays produced by the shape of the scan geometry. In order to eliminate the effects of the scan trajectory on the collected data, $\gamma(\omega',\varepsilon')$ must be removed from $S_p(\omega',\varepsilon')$. For this purpose, the following operation is performed:

$$U_p(\omega',\varepsilon') = S_p(\omega',\varepsilon') \cdot \gamma(\omega',\varepsilon')^{+} = S_p(\omega',\varepsilon') \cdot C(\omega',\varepsilon') \qquad (2.10)$$

where $\gamma(\omega',\varepsilon')^{+}$ denotes the complex conjugate of $\gamma(\omega',\varepsilon')$ and $C(\omega',\varepsilon') = \exp\left(j\cdot\left(\sqrt{4k'^2R^2-\varepsilon'^2}+\varepsilon'\cdot\sin^{-1}(\varepsilon'/2k'R)+\varepsilon'\pi\right)\right)$. The resulting spectrum is given by:

$$U_p(\omega',\varepsilon') = 4\sigma_p\cdot\zeta_p(\omega',\varepsilon')\cdot\exp\left(-j(\sqrt{4k'^2r'_p{}^2-\varepsilon'^2}+\varepsilon'\cdot\sin^{-1}(\varepsilon'/2k'r_p)+\varepsilon'\phi_p\right). \tag{2.11}$$

where $k'=\omega'/v$. The next step is to transfer the data in $U_p(\omega',\varepsilon')$, from the (ω',ε') frequency space to the (k'_x,k'_y) spatial frequency space, where k'_x and k'_y are the spatial frequency counterparts of x and y spatial domains. Next, the inverse FFT of the focused data is computed on the ε' direction, resulting in a representation of the collected data in the (ω', θ_n) domain. We will refer to the resulting spectrum as $U_p(\omega',\theta_n)$. At this point, a new frequency space, denoted as (k_{ux}, k_{uy}) is generated, where:

$$k_{ux} = k\cdot\cos(\theta_n) \tag{2.12}$$

$$k_{uy} = k\cdot\sin(\theta_n). \tag{2.13}$$

In order to migrate the spectral information contained in $U_p(\omega', \theta_n)$ to the (k_{ux}, k_{uy}) space, the mapping described in (2.12) and (2.13) is performed for the (ω',θ_n) plane. We call this new mapped spectrum $I_p(k_{ux}, k_{uy})$. The differences between adjacent samples in the (k_{ux}, k_{uy}) plane are not constant, resulting in a non uniformly sampled frequency space. In order to obtain an evenly sampled spectrum, a new discrete frequency space, denoted as (k'_x, k'_y), is defined. In this space the separation between samples is in each (k'_x, k'_y) plane is $\Delta k'_y=\Delta k'_x=\pi/R$. Next, the evenly sampled spectrum $I_p(k'_x,k'_y)$ is generated by interpolating the data contained in $I_p(k_{ux},k_{uy})$ into the frequency values specified in the (k'_x, k'_y) space. Finally, in order to visualize the reconstructed data in the spatial domain a 2D inverse FFT is applied to $I_p(k'_x, k'_y)$. The result of this process is the image $i_p(x_a, y_b)$, where a and b are the sample indexes along the x and y axis. A flow diagram of the reconstruction process can be seen in figure 2.4.

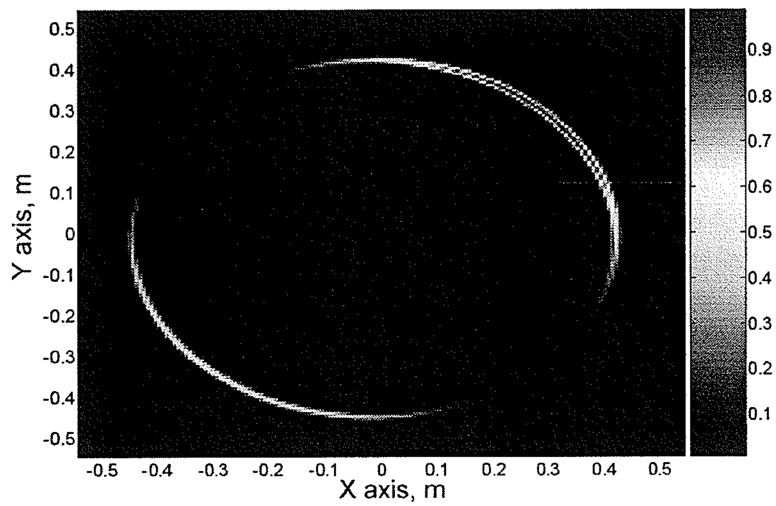

Figure 2.3. Uncompensated 2D image from a point scatter located at (0.02 m, 0.02 m).

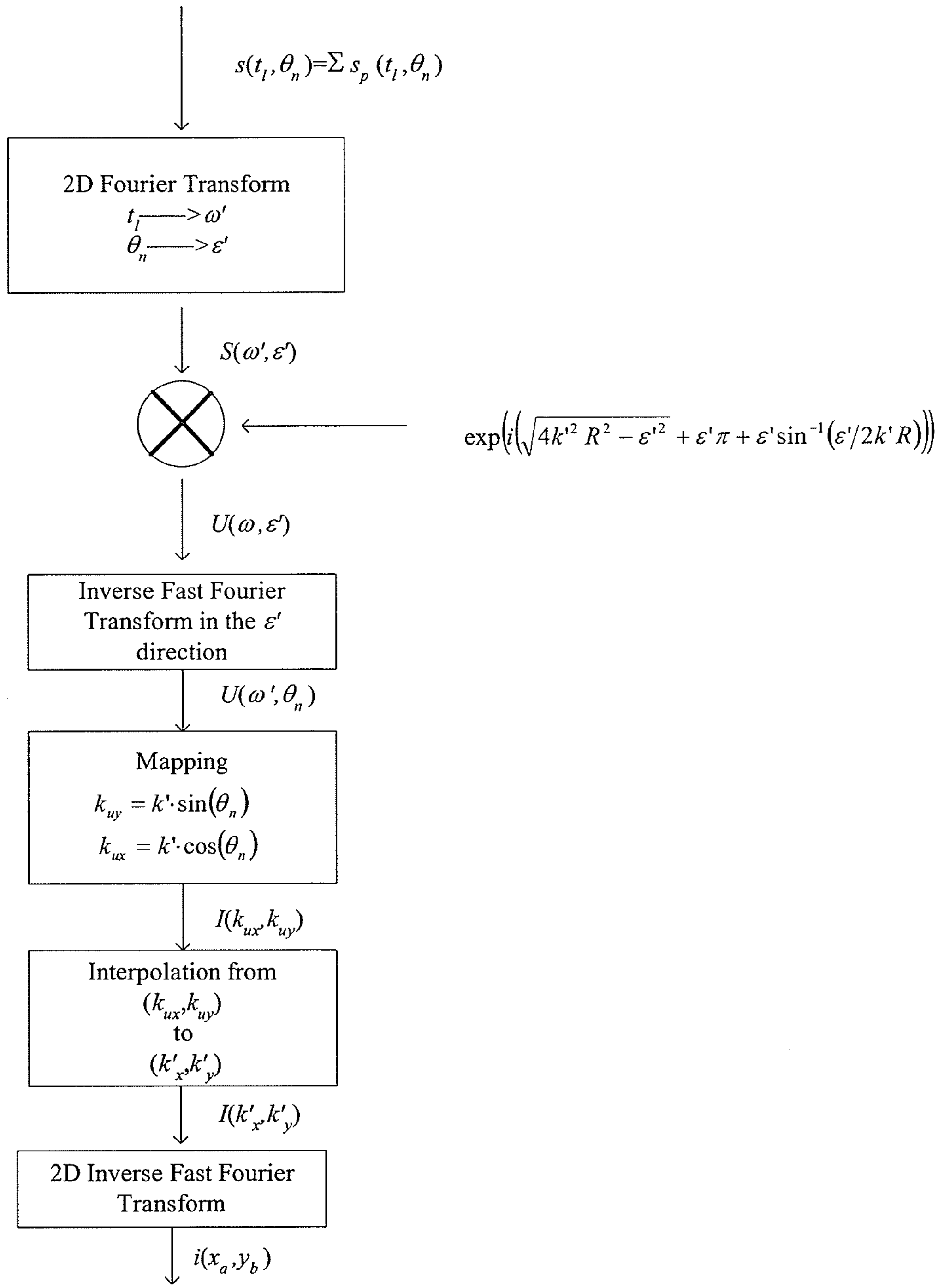

Figure 2.4. Flow diagram of the proposed reconstruction method for circular scan trajectories.

3. WAVEFRONT RECONSTRUCTION OF CYLINDRICAL SR DATA.

3.1 Signal model

For certain imaging scenarios, a 3D scan trajectory is required in order to properly visualize the targets present in the scan area. In this chapter, the generic cylindrical scan geometry signal model is analyzed. This scan trajectory is formed by a series of circular trajectories in the (x,y) plane stacked in a parallel fashion along the z axis. Each scan location is facing towards the center of its corresponding scan plane. T point scatterers are assumed to be located inside the area delimited by the scan trajectory. In this data acquisition geometry, the distance between the scan location at (R,θ,z) and the p^{th} scatter is:

$$L_p(\theta,z)=\sqrt{R^2+r_p^{\,2}+(z_p-z)^2-2\cdot R\cdot r_p\cos(\phi_p-\theta)} \text{ for } z \in [z_{\min}, z_{\max}],\ \theta\in[0,2\pi] \quad (3.1)$$

where (R, θ, z) are the coordinates of the scan location, $z_{\min}$ and z_{max} are the lower and upper spatial bounds of the scan trajectory along the azimuth direction and (r_p, ϕ_p, z_p) is the location of the p^{th} scatter . A diagram of the scan geometry can be seen in figure 3.1.

At each scan location, a waveform $f(t)$ is radiated and the responses from the targets within the scan area are recorded. For the scan location at (R, θ, z), the received signal can be expressed as:

$$s(t,\theta,z)=\sum_{q=1}^{T}\sigma_q f\left(t-\frac{2\cdot L_q(\theta,z)}{v}\right). \tag{3.2}$$

where once again v is the propagation speed on the medium and σ_q is the reflectivity of the q^{th} scatter. Let consider now the response from the p^{th} scatter:

$$s_p(t,\theta,z)=\sigma_p\cdot f\left(t-\frac{2\cdot L_p(\theta,z)}{v}\right). \tag{3.3}$$

The frequency representation of the previous signal can be obtained by calculating its Fourier transform, yielding the following expression:

$$S_p(\omega,\theta,z)=\sigma_p F_p(\omega)\exp\left(-j\left(2k\cdot L_p(\theta,z)\right)\right),\ \omega\in[\omega_{\min},\omega_{\max}] \tag{3.4}$$

where ω_{max} and ω_{min} are the maximum and minimum frequency components of the irradiated signal.

3.2 Spherical phase function analysis

As mentioned in the previous chapter, it is imperative to analyze the spectral behavior of the spf along the slow trajectories in order to determine the nature of the corresponding holographic focusing approach. The first step in this process is to calculate the Fourier transform of its spf along the θ and z scan directions. This operation is given by:

$$S_p(\omega,\varepsilon,k_z)=\int_0^{2\pi}\int_{z_{\min}}^{z_{\max}}\sigma_p F_p(\omega)\cdot\exp\left(-j\left(2k\cdot L_p(\theta,z)+\varepsilon\theta+k_z z\right)\right)dz\,d\theta \quad \text{for } k\in[\omega_{\min}/\nu,\omega_{\min}/\nu] \qquad (3.5)$$

where k_z is the spatial frequency counterpart of z.

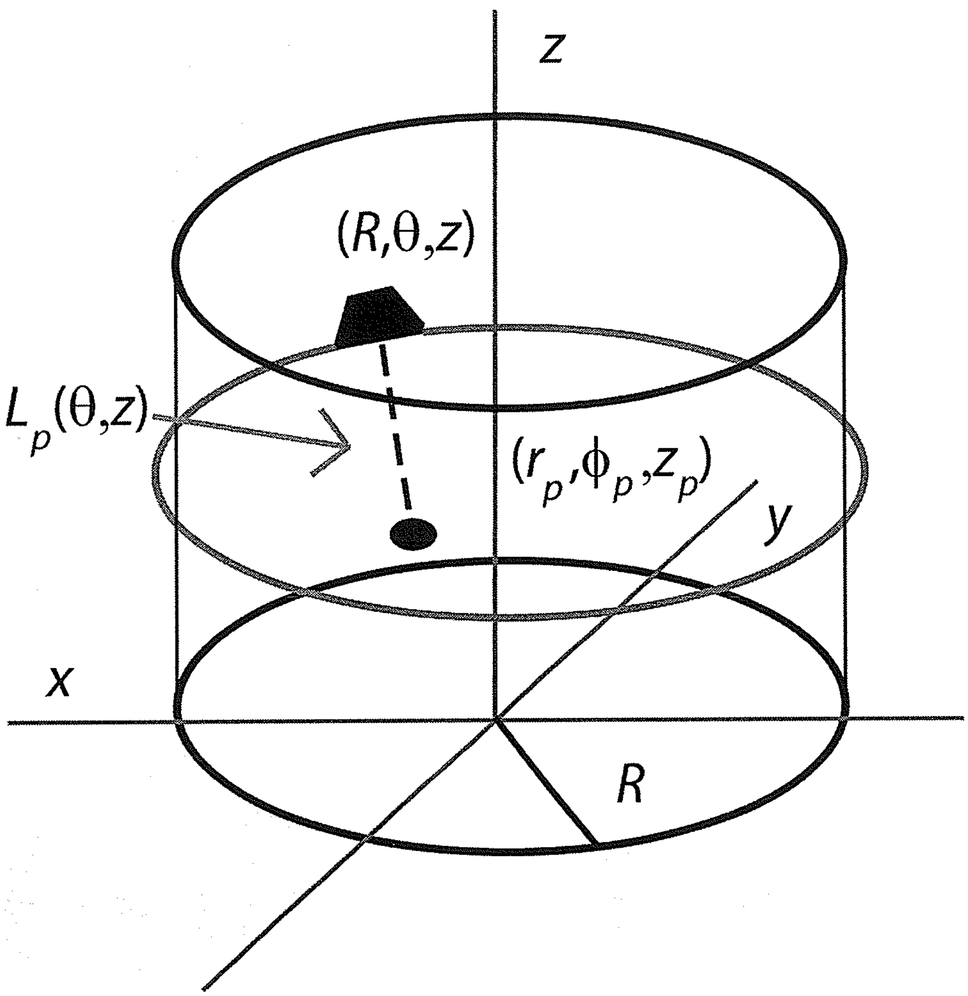

Figure 3.1. Diagram of the cylindrical scan trajectory.

Similarly to (2.4), (3.5) starts to oscillate rapidly around zero when k becomes large, making difficult to accurately calculate this integral. Nevertheless, the stationary phase method can be also used in 3D PM functions such as (3.5). In order to calculate the AB of the spf, the stationary points, z^* and θ_z^*, along the slow-time trajectories must be determined. In order to make this process easier to follow, the value of z^* will be calculated first. For the expression in (3.5), the IF in the z direction is given by:

$$\frac{\partial\left(-2k \cdot L_p(\theta,z)+\varepsilon\theta+k_z z\right)}{\partial z}=\frac{2k(z_p-z)}{\sqrt{R^2+r_p{}^2+(z_p-z)^2-2\cdot R\cdot r_p\cos(\phi_p-\theta)}}-k_z \cdot \tag{3.6}$$

The stationary point along the z direction, z^*, (3.6) is defined as:

$$\left[\frac{\partial\left(-2k \cdot L_p(\theta,z)+\varepsilon\theta+k_z z\right)}{\partial z}\right]_{z=z^*}=0 \cdot \tag{3.7}$$

By substituting (3.6) into (3.7), the following expression is obtained:

$$\frac{(z_p-z^*)}{\sqrt{R^2+r_p{}^2+(z_p-z^*)^2-2\cdot R\cdot r_p\cos(\phi_p-\theta)}}=\frac{k_z}{2k} \cdot \tag{3.8}$$

The determination of an analytical expression for z^* can be a tedious process. Nevertheless, notice how the left side of (3.8) resembles a trigonometric relationship. Taking advantage of this fact, (3.8) can be rewritten as:

$$\sin\left(\tan^{-1}\left(\frac{(z_p - z^*)}{\sqrt{R^2 + r_p^{\ 2} - 2\cdot R\cdot r_p \cos(\phi_p - \theta)}}\right)\right) = \frac{k_z}{2k}. \tag{3.9}$$

After an algebraic manipulation process, the following expression is obtained:

$$z^* = z_p - \frac{k_z}{\sqrt{4k^2 - k_z^2}}\sqrt{R^2 + r_p^{\ 2} - 2\cdot R\cdot r_p \cos(\phi_p - \theta)}. \tag{3.10}$$

Now that the value of z^* has been obtained, it will be used to determine the AB of (3.5) along the z direction. As mentioned in [25], in order to do this (3.5) must be evaluated at z^*. This operation is defined as:

$$S_p(\omega,\varepsilon,k_z) = 2\int_0^{2\pi} \sigma_p \cdot F_p(\omega)\cdot \exp\left(-j\left(2k\cdot L_p(\theta,z) + \varepsilon\theta + k_z z\right)\right)d\theta\Big|_{z=z^*}. \tag{3.11}$$

This yields:

$$S_p(\omega,\varepsilon,k_z) = 2\int_0^{2\pi} \sigma_p \cdot \Psi_p(\omega,k_z)\cdot \exp\left(-j\left(\sqrt{4k^2 - k_z^2}\,D_p(\theta) + \varepsilon\theta + k_z z_p\right)\right)d\theta \tag{3.12}$$

where $\Psi_p(\omega,k_z)$ is the spectrum amplitude component in the (ω,k_z) frequency space, Next, the asymptotic behavior in the θ direction must be determined in order to calculate the 3D spectrum of (3.5). In this case, the IF of the PM component of (3.12) in the θ direction is:

$$\frac{\partial\left(-\sqrt{4k^2-k_z^2}\,D_p(\theta)-\varepsilon\theta\right)}{\partial\theta}=-\frac{\sqrt{4k^2-k_z^2}\left(R\cdot r_p\sin(\phi_p-\theta)\right)}{D_p(\theta)}-\varepsilon\ . \qquad (3.13)$$

The stationary point θ_z^* is achieved when (3.13) is equal to zero. Therefore:

$$\left[-\frac{\sqrt{4k^2-k_z^2}\left(R\cdot r_p\sin(\phi_p-\theta)\right)}{\sqrt{R^2+r_p^2-2\cdot R\cdot r_p\cos(\phi_p-\theta)}}-\varepsilon\right]_{\theta=\theta_z^*}=0\ . \qquad (3.14)$$

By algebraically manipulating (3.14) the following relationship can be obtained:

$$\frac{\sin(\phi_p-\theta_z^*)}{\sqrt{R^2+r_p^2-2\cdot R\cdot r_p\cos(\phi_p-\theta_z^*)}}=-\frac{\varepsilon}{\sqrt{4k^2-k_z^2}\cdot R\cdot r_p}\ . \qquad (3.15)$$

Similarly to (2.8), it can be seen that (3.15) presents a relationship similar to the one expressed by the sine law. If we include all the remaining angles in the scan plane, α_z^* and β_z^*, the following expression is obtained:

$$\frac{\sin(\phi_p-\theta_z^*)}{\sqrt{R^2+r_p^2-2\cdot R\cdot r_p\cos(\phi_p-\theta_z^*)}}=\frac{\sin(\alpha_z^*)}{r_p}=\frac{\sin(\beta_z^*)}{R}=-\frac{\varepsilon}{\sqrt{4k^2-k_z^2}\cdot R\cdot r_p}\ . \qquad (3.16)$$

Furthermore, by manipulating (3.16), it can be shown that:

$$\alpha_z^*=-\sin^{-1}\left(\varepsilon/\left(\sqrt{4k^2-k_z^2}\,R\right)\right) \qquad (3.17)$$

$$\beta_z^* = -\sin^{-1}\left(\varepsilon / \left(\sqrt{4k^2 - k_z^2}\, r_p\right)\right) \quad . \tag{3.18}$$

Now that the values of α_z^* and β_z^* have been determined, the value of θ_z^* can be obtained by using basic trigonometry. Analogously to the expression for θ^* obtained in the previous chapter, the stationary point in the θ scan trajectory in a cylindrical scan geometry is given by $\theta_z^* = \phi_p + \alpha_z^* + \beta_z^* - \pi$. Next, the AB of (3.5) along the slow-time direction θ is obtained by evaluating (3.12) at θ_z^*. This resulting expression is:

$$\begin{aligned} S_p(\omega,\varepsilon,k_z) = 4\sigma_p \cdot \zeta_p(\omega,\varepsilon,k_z) \cdot \exp\Big[-j\Big(\sqrt{\left(4k^2 - k_z^2\right) r_p^{\,2} - \varepsilon^2} + \sqrt{\left(4k^2 - k_z^2\right) R^2 - \varepsilon^2} + \\ \varepsilon \cdot sin^{-1}\left(\varepsilon / \sqrt{4k^2 - k_z^2}\, R\right) + \varepsilon \cdot \sin^{-1}\left(\varepsilon / \sqrt{4k^2 - k_z^2}\, r_p\right) + \varepsilon\pi + \varepsilon\phi_p + k_z z_p\Big)\Big] \end{aligned} \tag{3.19}$$

where $\zeta_p(\omega,\varepsilon,k_z)$ is the spectrum amplitude component in the (ω,ε,k_z) frequency space. A formal proof regarding the use of (θ^*,z^*) as a valid stationary point is illustrated in the appendix II.

3.3 Image reconstruction

Similarly to circular scan geometries, the data acquisition process along cylindrical scan trajectories is performed in discrete steps. Therefore, the data set $s(t,\theta,z)$ takes the form of an evenly sampled discrete space. This discrete version of $s(t,\theta,z)$, $s(t_l,\theta_n,z_m)$, is defined over a $L \times M \times$ grid where M is the total number of scan planes along the z

axis, and m denotes the sample index along the z scan trajectory. Provided that the sampling process satisfies the Nyquist-Shannon theorem [27], the theoretical analysis shown in the last subsection is valid for the 3D discrete Fourier transform of $s(t_l,\theta_n,z_m)$, $S(\omega',\varepsilon',k'_z)$, where k'_z is the discrete counterpart of k_z.

The circular aperture has a very similar effect in the spectra of SR collected along cylindrical and circular scan trajectories. Similarly to (2.19), (3.19) can be decomposed in two kinds of elements. The first set, denoted as $\kappa_p(\omega',\varepsilon',k'_z)$, is the formed by the spectral components related to the target responses, and it is a function of the target location, (r_p,θ_p,z_p). The second type of spectral components, $\gamma(\omega',\varepsilon',k'_z)$, is formed by the terms related to the delays produced by the shape of the cylindrical scan aperture. In order to eliminate the effects of $\gamma(\omega',\varepsilon',k'_z)$ on $S_p(\omega',\varepsilon',k'_z)$, the following operation is performed:

$$U_p(\omega',\varepsilon',k'_z)=S_p(\omega',\varepsilon',k'_z)\cdot\gamma(\omega',\varepsilon',k'_z)^{+}=S_p(\omega',\varepsilon',k'_z)\cdot C(\omega',\varepsilon',k'_z) \tag{3.20}$$

where $\gamma(\omega',\varepsilon',k'_z)^{+}$ denotes the complex conjugate of $\gamma(\omega',\varepsilon',k'_z)$ and $C(\omega',\varepsilon',k'_z)=\exp\left(j\cdot\left(\sqrt{\left(4k'^2-k'^2_z\right)R^2-\varepsilon'^2}+\varepsilon'\cdot\sin^{-1}\left(\varepsilon'/\sqrt{4k'^2-k'^2_z}R\right)+\varepsilon'\pi\right)\right)$. The resulting spectrum is given by:

$$U_p(\omega',\varepsilon',k'_z)=4\sigma_p\cdot\zeta_p(\omega',\varepsilon',k'_z)\cdot\exp\left(-j\left(\sqrt{\left(4k'^2-k'^2_z\right)r'_p{}^2-\varepsilon'^2}+\varepsilon'\cdot\sin^{-1}\left(\varepsilon'/\sqrt{4k'^2-k'^2_z}r_p\right)+\varepsilon'\phi_p+k'_z z_p\right)\right). \tag{3.21}$$

The next step is to transfer the data in $U_p(\omega',\varepsilon',k'_z)$, from the $(\omega',\varepsilon',k'_z)$ frequency space to the (k'_x,k'_y,k'_z) spatial frequency space. For this purpose, the auxiliary function $k_{ur}(\omega',k'_z)=\sqrt{4k'^2-k'^2_z}$ will be used. Since k' and k'_z are evenly sampled, the differences between adjacent values within $k_{ur}(\omega',k'_z)$ vary across the grid in which the function is defined. As mentioned in [29], uneven sampled frequency spaces are unfit to be processed using FFT based techniques. In order to correct this issue, the function $k_{er}(l',k'_z)=l'\cdot\Delta k_r$ is defined, where $\Delta k_r=\pi/R$ and l' goes from 1 to L. Within $k_{er}(l',k'_z)$, the differences between the values present at adjacent samples is the same for all its domain grid. We will refer to the set of values present in $k_{er}(l',k_z)$ as the (k_r,k'_z) frequency space. In order to produce a spectrum suitable to be processed using FFT techniques, the data present in each (ω',k'_z) plane in $U_p(\omega',\varepsilon', k'_z)$ is interpolated into the frequency values specified in the (k_r,k'_z) space. This operation is performed for each plane in the ε' direction. The outcome of this process will be referred as $U_p(k_r,\varepsilon',k'_z)$. As shown figure 3.2, if this mapping process is not performed, the target signatures will present an overextended signature along the z axis.

Next, the inverse FFT of $U_p(k_r,\varepsilon',k'_z)$ is computed on the ε' direction, resulting in a representation of the collected data in the (k_r, θ_n, k'_z) domain. We will refer to the resulting spectrum as $U_p(k_r,\theta_n,k'_z)$. Analogously to the circular scan geometry case, a new frequency space, denoted as (k'_{ux},k'_{uy},k'_z) is generated, where:

$$k'_{ux}=k_r\cdot\cos(\theta_n) \tag{3.22}$$

$$k'_{uy}=k_r\cdot\sin(\theta_n). \tag{3.23}$$

In order to migrate the spectral information contained in $U_p(k_r, \theta_n, k'_z)$ to the (k'_{ux}, k'_{uy}, k'_z) space, the mapping described in (3.22) and (3.23) is performed for the (k_r, θ_n) plane corresponding to each k'_z value. We call this new mapped spectrum $I_p(k'_{ux}, k'_{uy}, k'_z)$. Similarly to $k_{ur}(\omega', k'_z)$, the differences between adjacent samples in the (k'_{ux}, k'_{uy}) plane are not constant, resulting in a non uniformly sampled frequency space. In order to obtain an evenly sampled spectrum, a new discrete frequency space, denoted as (k'_x, k'_y, k'_z), is defined. In this space the separation between samples is in each (k'_x, k'_y) plane is $\Delta k'_y = \Delta k'_x = \pi/R$. The next step is to generate the evenly sampled spectrum $I_p(k'_x, k'_y, k'_z)$ by interpolating the data contained in $I_p(k'_{ux}, k'_{uy}, k'_z)$ into the frequency values specified in the (k'_x, k'_y, k'_z) space. Finally, in order to visualize the reconstructed data in the spatial domain, the 3D inverse FFT of $I_p(k'_x, k'_y, k'_z)$ is calculated. The result of this operation is the 3D model $i_p(x_a, y_b, z_m)$. A flow diagram of the reconstruction process can be seen in figure 3.3.

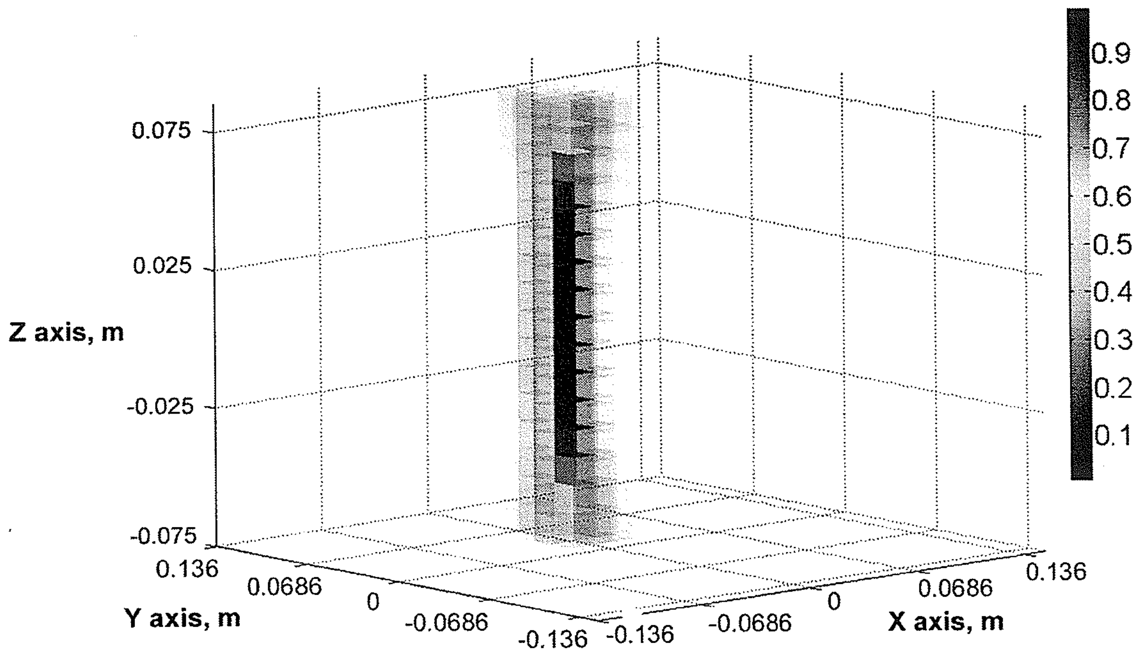

Figure 3.2. Scan plane-only focused target signature of a 1cm x 1cm x 1cm scatter at (0 cm, 2cm , 0 cm). The data was not focused along the z scan trajectory.

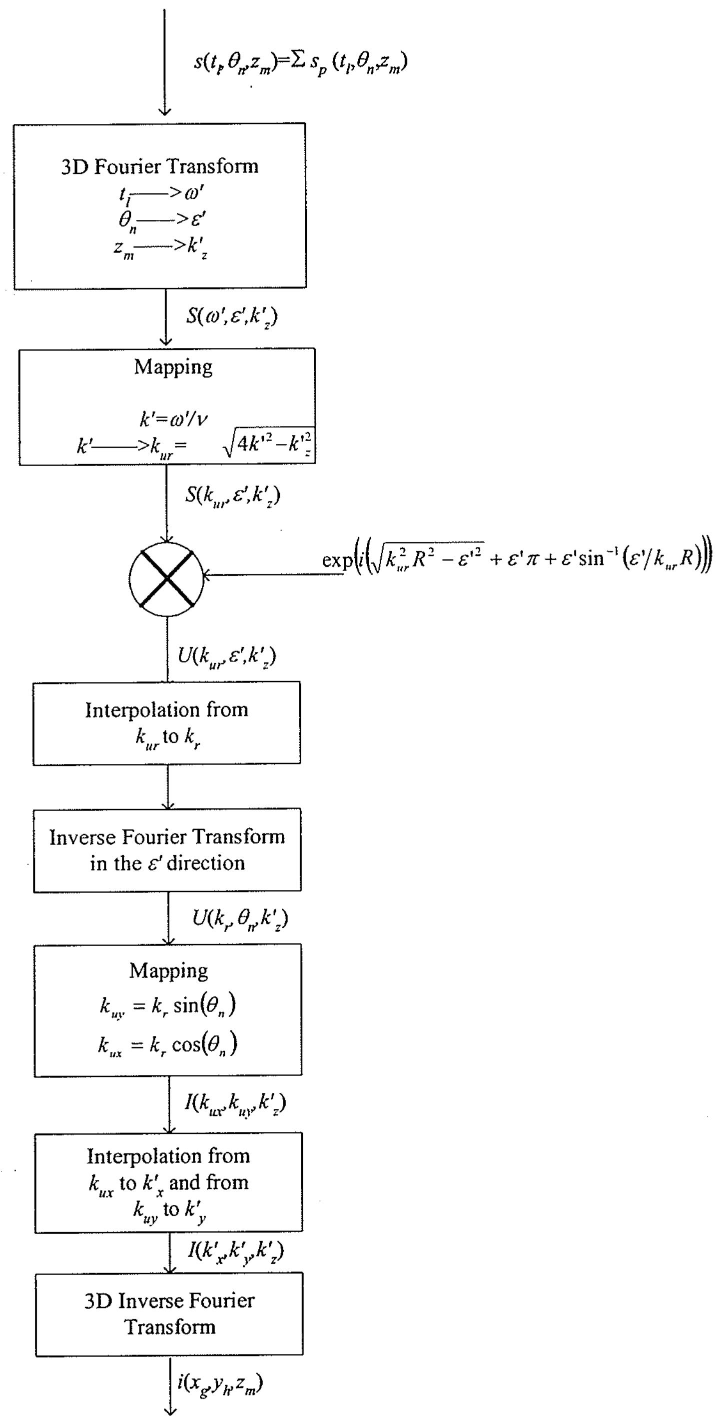

Figure 3.3. Flow diagram of the proposed focusing approach for SR data acquired along cylindrical scan trajectories.

4. POINT SPREAD FUNCTION CONSIDERATIONS

4.1 Overview

The psf of a radar system shows the extension of an ideal point scatter response in the spatial domain and is commonly used to determine the spatial resolvability of a radar system. As discussed in [8], the psf is directly related to the spatial bandwidth of the spf. In general, the point spread function of the p^{th} target along the w scan trajectory is defined as:

$$psf_p(\Omega_{w,p}, w) = |\Omega_{w,p}|sinc\left(\frac{\Omega_{w,p} \cdot w}{2\pi}\right) \qquad \text{for } p=1,2,..T \qquad (4.1)$$

where $\Omega_{w,p}$ is the support band of the collected responses of the target p along the w scan direction. It must be noted that the determination of (4.1) was made considering an ideal illumination scenario, where the radiation footprint of the active antenna satisfies the two basic conditions: *i*) it covers the whole scan area, and *ii*) it does not present any gain differences along its cross region. Although in realistic scenarios (4.1) still holds as a valid approximation, the size of the support band becomes dependant of the antenna radiation pattern characteristics. If the ideal illumination conditions are not met, the psf becomes a function of the antenna beamwidth size and it may vary between targets with similar support band values [8, 30]. In practice, this value is often approximated by calculating the range of support of the corresponding sinc function, which is given by the width of its mainlobe. For the psf shown in (4.1), the mainlobe width, Δw_p, is given by $\Delta w_n = 2\pi / |\Omega_p(k_w)|$.

In order to define the psf for a radar system, the support band in each scan direction must be determined. As shown in [8] and [31], the support band corresponding to the t scan direction is the same for all the targets in the scan area, or in other words, $|\Omega_{t,p}| = B$, where B is the bandwidth of the emitted waveform. Furthermore, because all radar signal models are a function of t, the values of Δt_p and $psf_p(B,t)$ are well known [8, 31]. The psf function of a radar signal in the t direction is given by:

$$psf_p(B,t) = \frac{4\pi B}{v} sinc\left(\frac{B \cdot t}{v}\right). \tag{4.2}$$

The spatial resolution achieved by this psf is equal to:

$$\Delta t_p = \frac{v}{2B}. \tag{4.3}$$

For the slow-time scan directions, the support bands are a function of the spatial frequencies collected along the scan trajectory, which may vary considerably between different scan patterns. In the following discussion, the support bands in the θ and z trajectories are determined. The corresponding psf and resolution values in both slow-time trajectories are calculated and the corresponding sampling requirements are explained.

4.2 Angular scan trajectory considerations

The support band of a PM signal can be determined by calculating the maximum and minimum IF values [8]. Since the circular scan trajectory spf given by (2.3) is a specific case of (3.4), the spf of a cylindrical scan geometry will be analyzed. For the generic cylindrical scan geometry spf, the IF along the θ scan direction is given by:

$$\frac{\partial\left(-2k\sqrt{R^2+r_p^2+(z_p-z)^2-2\cdot R\cdot r_p\cos(\phi_p-\theta)}\right)}{\partial\theta}=\frac{2k\cdot R\cdot r_p\sin(\phi_p-\theta)}{\sqrt{R^2+r_p^2+(z_p-z_a)^2-2\cdot R\cdot r_p\cos(\phi_p-\theta)}}. \tag{4.4}$$

This shows that IF in the θ scan direction is a function of the target location. The maximum IF value with respect to θ is achieved at :

$$\max(\phi_p-\theta_n)=\cos^{-1}\left(\frac{\chi(R,r_p,z_p-z)-\sqrt{\chi(R,r_p,z_p-z)^2-4}}{2}\right) \tag{4.5}$$

where:

$$\chi(R',r',z')=\frac{R'^2+r'^2+(z')^2}{R'\cdot r'} \tag{4.6}$$

and the corresponding IF value is:

$$\left[\frac{d\left(-2k\sqrt{R^2+r_p^2+(z_p-z)^2-2R\cdot r_p\cos(\phi_p-\theta)}\right)}{d\theta}\right]_{(\phi_p-\theta)=(\phi_p-\theta_n)^*}=\frac{2kRr_p\sin(\phi_p-\theta)^*}{\sqrt{R^2+r_p^2+(z_p-z_a)^2-2R\cdot r_p\cos(\phi_p-\theta)^*}}\,. \quad (4.7)$$

Similarly, it can be shown that the minimum IF value with respect to θ is achieved when $(\phi_p-\theta_n)=2\pi-(\phi_p-\theta_n)^*$. The corresponding IF in this case is

$$\left[\frac{d\left(-2k\sqrt{R^2+r_p^2+(z_p-z_n)^2-2R\cdot r_p\cos(\phi_p-\theta_n)}\right)}{d\theta}\right]_{(\phi_p-\theta)=2\pi-(\phi_p-\theta)^*}=-\frac{2kRr_p\sin(\phi_p-\theta)^*}{\sqrt{R^2+r_p^2+(z_p-z_a)^2-2R\cdot r_p\cos(\phi_p-\theta)^*}}\,. \quad (4.8)$$

Therefore, the support band $\Omega_{\theta,p}$ in the θ scan direction for the p^{th} target is given by:

$$\Omega_{\theta,p}=\frac{2kRr_p\sin(\phi_p-\theta)^*}{\sqrt{R^2+r_p^2+(z_p-z)^2-2R\cdot r_p\cos(\phi_p-\theta)^*}}-\frac{-2kRr_p\sin(\phi_p-\theta)^*}{\sqrt{R^2+r_p^2+(z_p-z)^2-2R\cdot r_p\cos(\phi_p-\theta)^*}}\,. \quad (4.9)$$

$$\Omega_{\theta,p}=\frac{4kRr_p\sin(\phi_p-\theta)^*}{\sqrt{R^2+r_p^2+(z_p-z)^2-2R\cdot r_p\cos(\phi_p-\theta)^*}}$$

Unlike $\Omega_{t,p}$, $\Omega_{\theta,p}$ is not the same for all the targets in the scan area, since it is a function of the target location and the scan plane. Nevertheless, under ideal illumination conditions, an accurate estimate of the psf mainlobe width can be calculated by using the center value of the domains of k,r_p and (z_p-z) [32]. For a set of fixed R, ν and B values, the estimated resolution corresponding to this support band is given by:

$$\Delta\theta(r_i, z_i) = \frac{\nu \cdot \sqrt{R^2 + (r_i/2)^2 + (z_i/2)^2 - 2R \cdot (r_i/2)\cos(\varphi)}}{4 \cdot f_c \cdot R \cdot (r_i/2) \cdot \sin(\varphi)} = \frac{\lambda_c \cdot \sqrt{R^2 + (r_i/2)^2 + (z_i/2)^2 - 2R \cdot (r_i/2)\cos(\varphi)}}{4 \cdot R \cdot (r_i/2) \cdot \sin(\varphi)} \tag{4.10}$$

where z_i and r_i are the height and radius of the scan area respectively, f_c is the center frequency of the emitted signal, $\lambda_c = \nu / f_c$ and:

$$\varphi = \cos^{-1}\left(\frac{\chi(R, r_i/2, z_i/2) - \sqrt{\chi(R, r_i/2, z_i/2)^2 - 4}}{2} \right). \tag{4.11}$$

If the antenna radiation footprint does not totally covers the scan area, $\Omega_{\theta,p}$ becomes a function of the antenna beamwidth size, ϑ=[ϑ_θ, ϑ_z], where ϑ_θ and ϑ_z are the antenna beamwidth sizes in the θ and z directions [8, 30]. In this case, the average resolution along the θ direction is equal to:

$$\Delta\theta(\vartheta_\theta, \vartheta_z) = \frac{\nu \cdot \sqrt{R^2 + (\vartheta_\theta/2)^2 + (\vartheta_z/2)^2 - 2R \cdot (\vartheta_\theta/2)\cos(\rho)}}{4 \cdot f_c \cdot R \cdot (\vartheta_\theta/2) \cdot \sin(\rho)} = \frac{\lambda_c \cdot \sqrt{R^2 + (\vartheta_\theta/2)^2 + (\vartheta_z/2)^2 - 2R \cdot (\vartheta_\theta/2)\cos(\rho)}}{4 \cdot R \cdot (\vartheta_\theta/2) \cdot \sin(\rho)} \tag{4.12}$$

where:

$$\rho = \cos^{-1}\left(\frac{\chi(R, \vartheta_\theta/2, \vartheta_z/2) - \sqrt{\chi(R, \vartheta_\theta/2, \vartheta_z/2)^2 - 4}}{2} \right). \tag{4.13}$$

Finally, in order to avoid the presence of aliasing along the θ scan direction in the collected data, the maximum spacing between scan locations in this slow-time direction must be set in such a way that the Nyquist sampling criterion is satisfied. For this purpose, the maximum value that $\Omega_{\theta,p}$ can possibly achieve must be determined, within the limits imposed by the scan trajectory. A simple way of determining this value is by substituting the upper bound values of the domains of the k,r_p and (z_p-z_a) variables into the right side of (4.9). The resulting expression is:

$$\left[\frac{2kRr_p \cdot \sin(\phi_p - \theta)}{\sqrt{R^2 + r_p^2 + (z_p - z)^2 - 2R \cdot r_p \cos(\phi_p - \theta)}}\right]_{k=k_m, r_p=r_i, (z_p-z)=z_i, (\phi_p-\theta)=\varphi} = \frac{2k_m R \cdot r_i \cdot \sin(\varphi)}{\sqrt{R^2 + r_i^2 + z_i^{\,2} - 2R \cdot r_p \cos(\varphi)}} \quad .(4.14)$$

where k_m is the maximum wavenumber value present in the emitted signal. Therefore, the angular separation between adjacent scan locations along the θ scan direction, $\delta\theta$, must satisfy the following criterion:

$$\delta\theta \leq \frac{2\pi\sqrt{R^2 + r_i^{\,2} + z_i^{\,2} - 2R \cdot r_i \cos(\varphi)}}{4k_m R \cdot r_i \cdot \sin(\varphi)} = \frac{\lambda_m \sqrt{R^2 + r_i^{\,2} + z_i^{\,2} - 2R \cdot r_i \cos(\varphi)}}{4R \cdot r_i \cdot \sin(\varphi)} \qquad (4.15)$$

where λ_m is the minimum wavelength present in the radiated signal. The previous analysis is also valid for circular scan geometries by substituting z_i=0 into the appropriate term.

In order to illustrate the effects of the psf in the reconstructed imagery, a pair of data sets containing two targets was generated using the radar signal simulator described in [32]. This simulation approach is based on the radar signal model proposed in [8]. It has a spatial and magnitude accuracy similar to the one obtained by finite difference time domain simulation approaches on imaging scenarios where the propagation medium has a homogeneous nature.

The size of each target was (0.013 m, 0.013 m, 0.01 m). The bandwidth of the simulated radar signal was 0-11 GHz. The simulated reflections were collected at 200 scan positions along 21 scan planes by 1 cm. The antenna beamwidth size was ϑ=[0.3 m, 0.12 m]. The simulated antenna beamwidth pattern was $\cos(\varpi_z)$ and $\cos(\varpi_\theta)$ along the z and θ directions respectively, where ϖ_z and ϖ_θ are the angles between the antenna center and the target in the z and θ axis. This antenna radiation pattern completely covers the scan area along the θ scan trajectory. The radius of the simulated scan pattern is 40 cm. In the first set, the scatters are located at (0.025 m, 0 m, 0.0 m) and (0.0205 m, 0.0143 m, 0.0 m) and in the second set they are located at (0.025 m, 0 m, 0.0 m) and (0.0220 m, 0.0119m, 0.0 m). As it can be seen in figure 4.1 a), the target signatures can be to properly visualized in the first case, due to the fact that the separation between targets is equal to the average resolution in the θ scan direction (1.1Δz(0.05m,0.12m)=0.6067 rad). On the contrary, in figure 4.1 b) the angular separation between the targets on the second set is equal to 0.9Δz(0.05m,0.12m)=0.4964 rad, causing an overlapping of the target signatures that makes difficult to properly visualize and interpret the reconstructed image. A series of simulated scenarios showing the radar reflections of two point targets at different locations separated by $1.1\,\Delta\theta(r_i, z_i)$ and $0.9\,\Delta\theta(r_i, z_i)$ at different radius of interest is shown in figure 4.2.

4.3 Azimuth scan trajectory considerations

Considering the response from the p^{th} scatter from (3.4), the IF of the PM term with respect to z is:

$$\frac{\partial\left(-2k\sqrt{R^2+r_p^2+\left(z_p-z\right)^2-2\cdot R\cdot r_p\cos(\phi_p-\theta_n)}\right)}{\partial z}=\frac{2k\cdot\left(z_p-z\right)}{\sqrt{R^2+r_p^2+\left(z_p-z\right)^2-2\cdot R\cdot r_p\cos(\phi_p-\theta)}}\;. \tag{4.16}$$

And its corresponding support band is:

$$\Omega_{z,p}=\frac{2k\cdot\left(z_p+z_i/2\right)}{\sqrt{R^2+r_p^2+\left(z_p+z_i/2\right)^2-2\cdot R\cdot r_p\cos(\phi_p-\theta)}}-\frac{2k\cdot\left(z_p-z_i/2\right)}{\sqrt{R^2+r_p^2+\left(z_p-z_i/2\right)^2-2\cdot R\cdot r_p\cos(\phi_p-\theta)}}\;. \tag{4.17}$$

In this case the support band is also a function of the target location and the scan angle. Similarly to the situation in the θ scan direction, the center values of the domains of k,r_p,(z_p-z) and (ϕ_p-θ) can be used to define an average value for the support band under ideal illumination conditions. The estimated mainlobe width for a set of fixed R, v, and B values in the z direction is equal to:

$$\Delta z(r_i,z_i)=\frac{v\cdot\sqrt{R^2+(r_i/2)^2+(z_i/2)^2}}{4\cdot f_c\cdot(z_i)}=\frac{\lambda_c\cdot\sqrt{R^2+(r_i/2)^2+(z_i/2)^2}}{4\cdot(z_i)} \tag{4.18}$$

where λ_c=v/f_c.

If the antenna radiation footprint does not cover completely the scan area, the average resolution in the z scan trajectory is equal to:

$$\Delta z(\vartheta_\theta, \vartheta_z) = \frac{v \cdot \sqrt{R^2 + (\vartheta_\theta/2)^2 + (\vartheta_z/2)^2}}{4 \cdot f_c \cdot (\vartheta_z/2)} = \frac{\lambda_c \cdot \sqrt{R^2 + (\vartheta_\theta/2)^2 + (\vartheta_z/2)^2}}{4 \cdot (\vartheta_z/2)}. \tag{4.19}$$

Finally, in order to satisfy the Nyquist criterion across the z scan trajectory, the spacing between scan planes, δz, must satisfy the following condition:

$$\delta z \leq \frac{2\pi\sqrt{R^2 + r_i^2 + z_i^2}}{4k_m z_i} = \frac{\lambda_m\sqrt{R^2 + r_i^2 + z_i^2}}{4R \cdot z_i}. \tag{4.20}$$

Similarly to the θ scan trajectory case, two sets of simulated radar signals where generated in order to show the psf considerations previously explained. Both data sets contained a pair of targets. The size of each target was (0.013 m, 0.013 m, 0.01 m). The bandwidth of the simulated radar signal was 0-11 GHz. The simulated reflections were collected at 200 scan positions along 21 scan planes by 1cm. The antenna beamwidth size was ϑ=[0.3 m, 0.12 m]. The simulated antenna beamwidth pattern was $\cos(\varpi_z)$ and $\cos(\varpi_\theta)$ along the z and θ axis respectively. The radius of the simulated scan pattern is 40 cm. In the first set, the scatters are located at (0.025 m, 0 m, -0.0309 m) and (0.025 m, 0 m, 0.02 m). In this data set, the azimuth separation between targets is 1.1Δz(0.1m, 0.12m) = 0.0509m. In the second set they are located at (0.025 m, 0 m, -0.0217m) and (0.025 m, 0 m, 0.02 m). In this data set, the azimuth separation between targets is 0.9Δz(0.1m, 0.12m)=0.0417m. The 3D reconstructed models corresponding to the first and second simulated data sets are shown in figure 4.3 a) and b) respectively. An additional series of simulated examples is shown in figure 4.4.

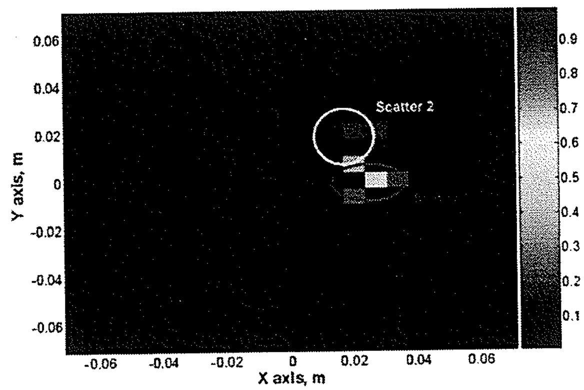

a)

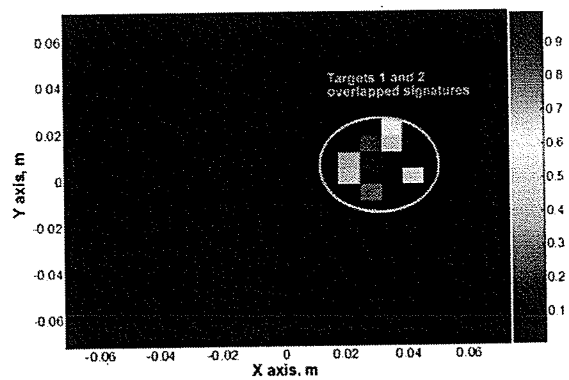

b)

Figure 4.1. Simulated data sets with an angular separation between targets of 1.1 $\Delta\theta(0.05,0.1)$ m and $0.9\Delta\theta(0.05,0.1)$m.

a) Reconstructed image from 2 point scatters located at: 1) (0.025 m, 0.0 m, 0.0 m) and 2) (0.0205 m, 0.0143 m, 0.0 m). The angular separation between targets is 1.1 $\Delta\theta(0.05,0.1)$ =0.6067 rad. $\Delta\theta(0.05,0.1)$=.5515 rad.

b) Reconstructed image from 2 point scatters located at: 1) (0.025 m, 0.0 rad, 0.0 m) and 2(0.0220 m, 0.0119m, 0.0 m). The angular separation between targets is $0.9\Delta\theta(0.05,0.1)$ =0.4964 rad.

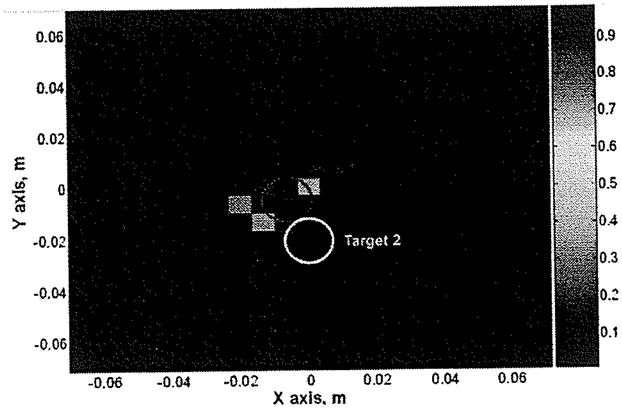

a)

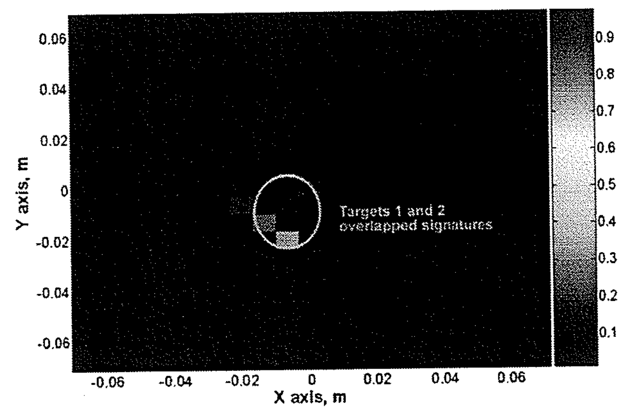

b)

Figure 4.2. Simulated data sets with an angular separation between targets of $1.1\,\Delta\theta(r_i, z_i)$ and $0.9\,\Delta\theta(r_i, z_i)$. Assorted locations.

a) Reconstructed image from 2 point scatters located at: 1) (-0.0138 m, -0.0145 m, 0.04 m) and 2) (0 m, -0.02 m, 0.04m). The angular separation between targets is 1.1 $\Delta\theta$(0.04,0.1) =0.7584 rad. $\Delta\theta$(0.04,0.1)=0.6895 rad.

b) Reconstructed image from 2 point scatters located at: 1) (-0.01160 m, -0.01630 m, 0.04 m) and 2) (0 m, -0.02 m, 0.04m). The angular separation between targets is 0.9$\Delta\theta$(0.04,0.1) =0.6205 rad

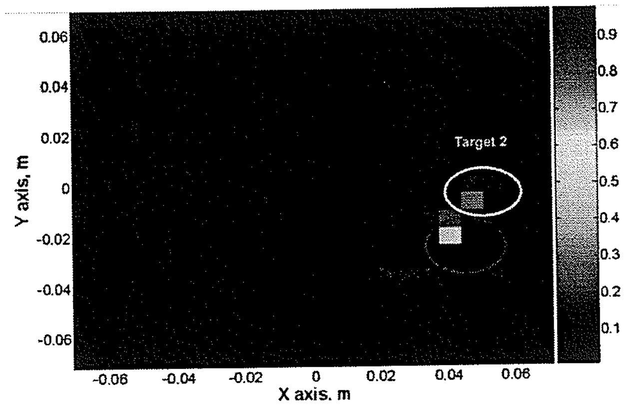

c)

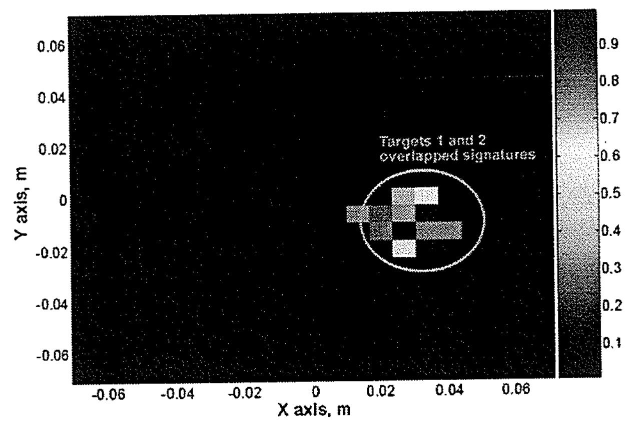

d)

Figure 4.2. Simulated data sets with an angular separation between targets of $1.1\,\Delta\theta(r_i, z_i)$ and $0.9\,\Delta\theta(r_i, z_i)$. Assorted locations.

c) Reconstructed image from 2 point scatters located at: 1) (0.05916 m, -0.03 m, -0.03 m) and 2) (0.05863 m, -0.01276 m, -0.03 m). The angular separation between targets is $1.1\Delta\theta(0.1,0.1)=0.3034$ rad. $\Delta\theta(0.1,0.1)=0.2758$ rad.

d) Reconstructed image from 2 point scatters located at: 1) (0.05916 m, -0.03 m, -0.03 m) and 2) (0.05782 m, -0.01603 m, -0.03 m). The angular separation between targets is $0.9\Delta\theta(0.1,0.1)=0.2482$ rad.

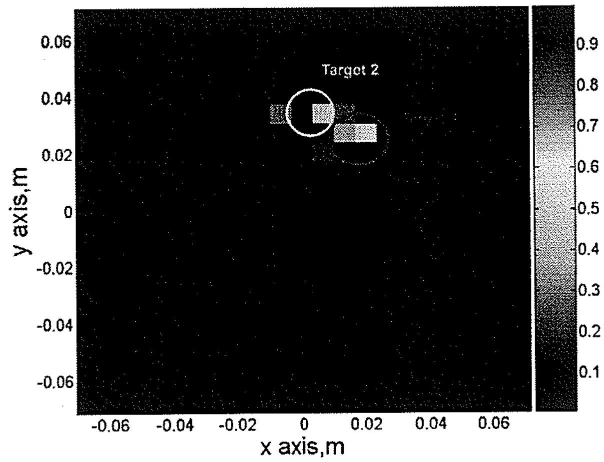

e)

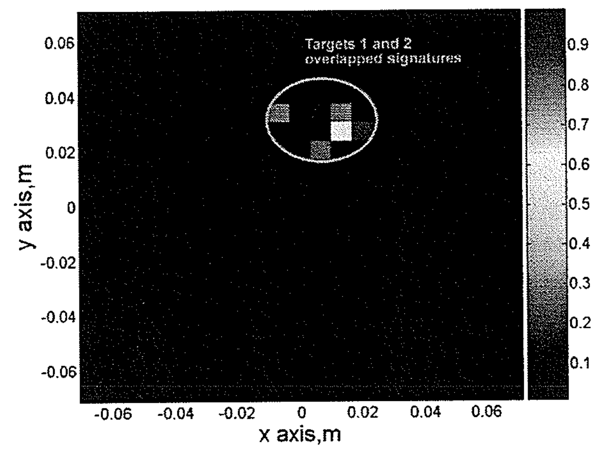

f)

Figure 4.2. Simulated data sets with an angular separation between targets of $1.1\,\Delta\theta(r_i, z_i)$ and $0.9\,\Delta\theta(r_i, z_i)$. Assorted locations.

e) Reconstructed image from 2 point scatters located at: 1) (0.0145 m, 0.0262 m, -0.01 m) and 2) (0 m, 0.03 m, -0.01 m). The angular separation between targets is 1.1 $\Delta\theta$(0.06,0.1)= 0.55 rad. $\Delta\theta$(0.06,0.1)=0.5 rad.

f) Reconstructed image from 2 point scatters located at: 1) (0.0121 m , 0.0275 m, -0.01 m) and 2) (0 m, 0.03 m, -0.01 m). The angular separation between targets is 0.9$\Delta\theta$(0.06m,0.1m)=0.45 rad.

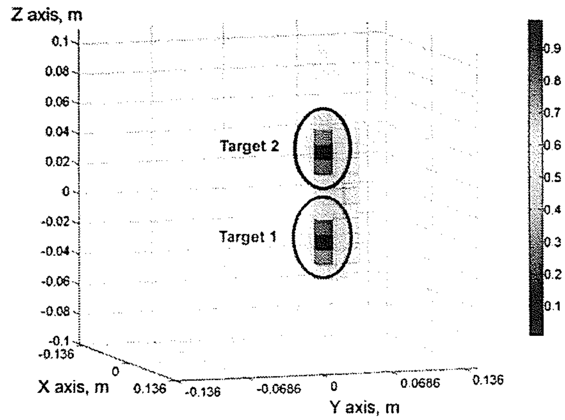

a)

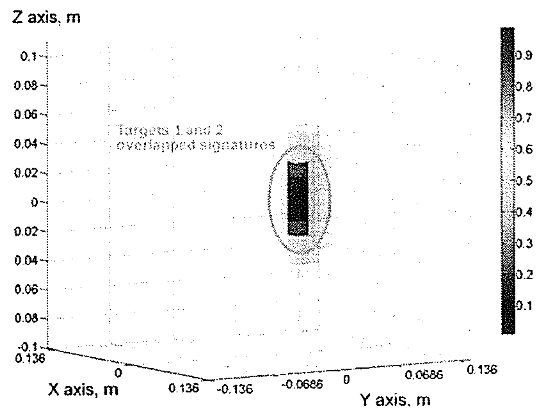

b)

Figure 4.3. Simulated data sets with an angular separation between targets of 1.1 $\Delta z(0.1\text{ m},0.12\text{ m})$ and 0.9 $\Delta z(0.1\text{ m},0.12\text{m})$. $\Delta z(0.1\text{ m},0.12\text{ m})=0.0463$ m.

a) Reconstructed image from 2 point scatters located at: 1) (0.025 m, 0 m, -0.0309 m) and 2) (0.025 m, 0 m, 0.02 m).The azimuth separation between targets is $1.1\Delta z(0.1\text{m},0.12\text{m})=0.0509$ m.

b) Reconstructed image from 2 point scatters located at: 1) (0.025 m, 0 m, -0.0217 m) and 2) (0.025 m, 0 m, 0.02 m). The azimuth separation between targets is $0.9\Delta z(0.1\text{m},0.12\text{m})=0.0417$ m.

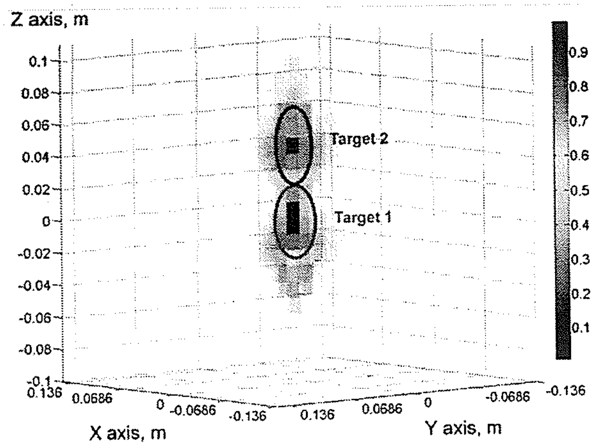

a)

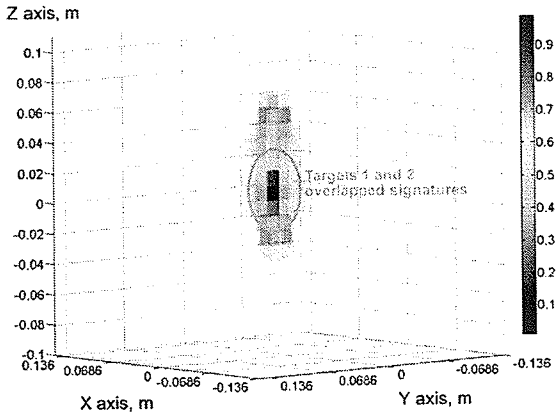

b)

Figure 4.4. Simulated data sets with an angular separation between targets of $1.1\,\Delta z(r_i, z_i)$ and $0.9\,\Delta z(r_i, z_i)$. Assorted locations. Δz(0.1 m,0.12 m)=0.0463 m.

a) Reconstructed image from 2 point scatters located at: 1) (-0.2828 m, 0.2828 m, -0.01 m) and 2) (-0.2828 m, 0.2828 m, 0.0409 m). The azimuth separation between targets is 1.1Δz(0.1 m,0.12 m)=0.0509 m.

b) Reconstructed image from 2 point scatters located at: 1) (-0.2828 m, 0.2828 m, -0.01 m) and 2) (-0.2828 m, 0.2828 m, 0.0317 m). The azimuth separation between targets is 0.9Δz(0.1 m,0.12 m)=0.0417 m. The azimuth separation between targets is 0.9Δz(0.1 m,0.12 m)=0.0417 m.

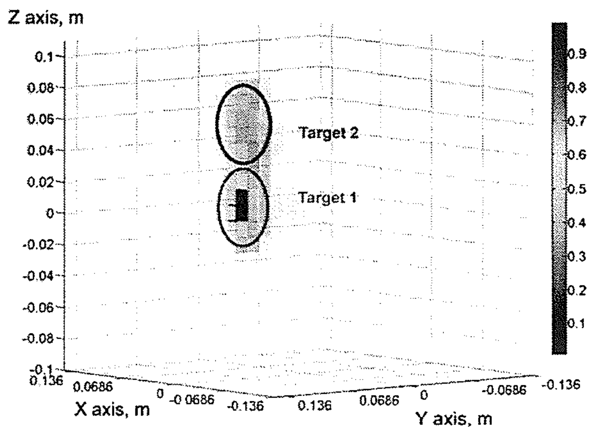

c)

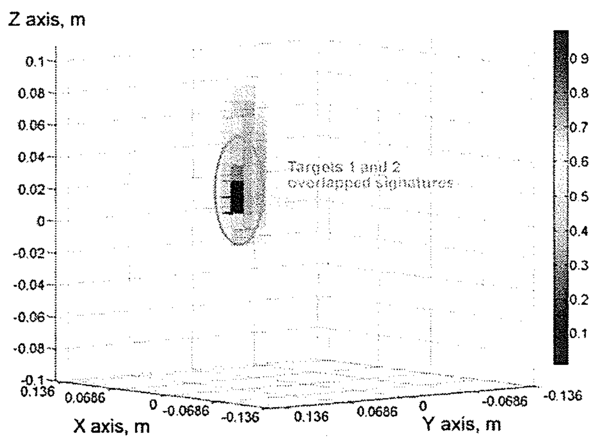

d)

Figure 4.4 Simulated data sets with an angular separation between targets of $1.1\,\Delta z(r_i, z_i)$ and $0.9\,\Delta z(r_i, z_i)$. Assorted locations. Δz(0.1 m,0.12 m)=0.0463 m.

c) Figure 4.4. Reconstructed image from 2 point scatters located at: 1) (0 m, 0.03 m, 0 m) and 2) (0 m, 0.03 m, -0.0509 m). The azimuth separation between targets is 1.1Δz(0.1 m,0.12 m)=0.0509 m.

d) Reconstructed image from 2 point scatters located at: 1) (0 m, 0.04 m, 0 m) and 2) (0 m, 0.04 m, 0.0417 m). The azimuth separation between targets is 0.9Δz(0.1 m,0.12 m)=0.0417 m.

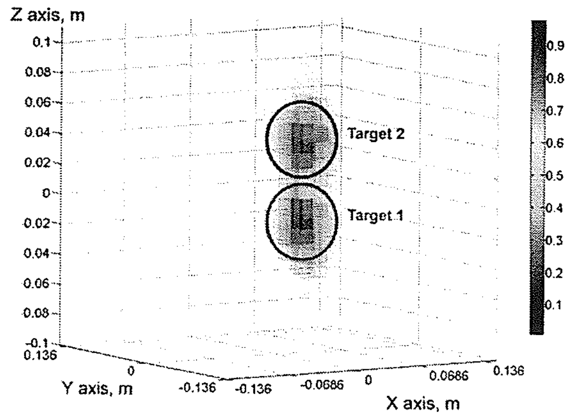

e)

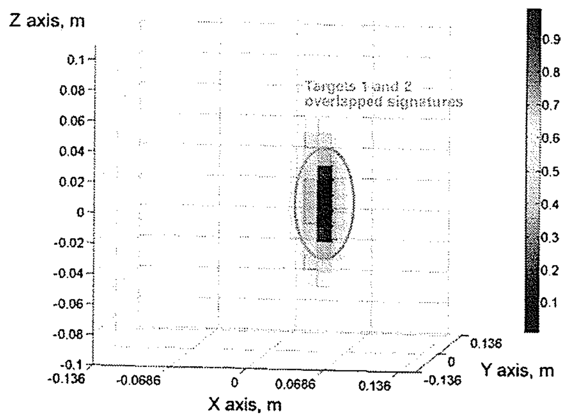

f)

Figure 4.4. Simulated data sets with an angular separation between targets of $1.1\,\Delta z(r_i, z_i)$ and $0.9\,\Delta z(r_i, z_i)$. Assorted locations. Δz(0.1 m,0.12 m)=0.0463 m.

e) Reconstructed image from 2 point scatters located at: 1) (0 m, 0.05 m,-0.0259 m) and 2) (0 m, 0.05 m, 0.025 m). The azimuth separation between targets is 1.1Δz(0.1 m,0.12 m)=0.0509 m.

f) Reconstructed image from 2 point scatters located at: 1) (0.025 m, -0.0433 m, -0.0167 m) and 2) (0.025 m, -0.0433 m, 0.025 m). The azimuth separation between targets is 0.9Δz(0.1 m,0.12 m)=0.0417 m.

5. RESULTS

5.1 2D Data acquisition system description

In order to test the proposed method, a SFCW Radar system was used. The system consists on a 360B Wiltron Network Analyzer and an AEL H Horn Antenna with a length of 19 cm and a height of 12 cm. A bandwidth of 11 GHz (1-12 GHz) was used in all the experiments. The system was characterized by recording the antenna responses inside an anechoic chamber. This reference signal was subtracted from the experiment data in order to eliminate distortions introduced by the components of the system. The data acquisition setup was surrounded by absorbing material in order to reduce undesirable environment reflections. The data was reconstructed using a 3 GHz PC with 1 GB RAM.

TABLE 5.1

Permittivity values of the materials used in the phantoms

Material	**Permittivity Value (E_r) at 6 GHz**
PVC	3
Air	1
Wood	1.7-1.8

5.2 Circular experiments.

For circular scans, a phantom similar to the one used in [23] was employed. This phantom consisted of a PVC pipe filled with air. The PVC pipe has a diameter of 10 cm and a height of 50 cm. Wood dowels are used as targets. The dowels have a 1.2 cm diameter. The phantom materials have almost no variation in their dielectric permittivity values in the 1-12 GHz frequency range. As it can be seen in Table 5.1, the contrast between air and wood is 1.8:1. The phantom and the experiment area can be observed in figure 5.1.

The data acquisition process was performed by rotating the phantom at 5° intervals for a total of 72 positions. At each position, the phantom was irradiated and the collected reflections were recorded. In order to allow a beamwidth coverage in all the scan positions and reduce undesirable interferences of antenna early time artifacts, the distance between the antenna and the center of the phantom is 70 cm. For the Fourier processing of the wavefront reconstructed data, a zero padding factor of 3 was used to improve the visualization of the reconstructed images. In the following discussion, the center of the phantom will be denoted as the origin, and the displayed images show the normalized energy of the reconstructed data.

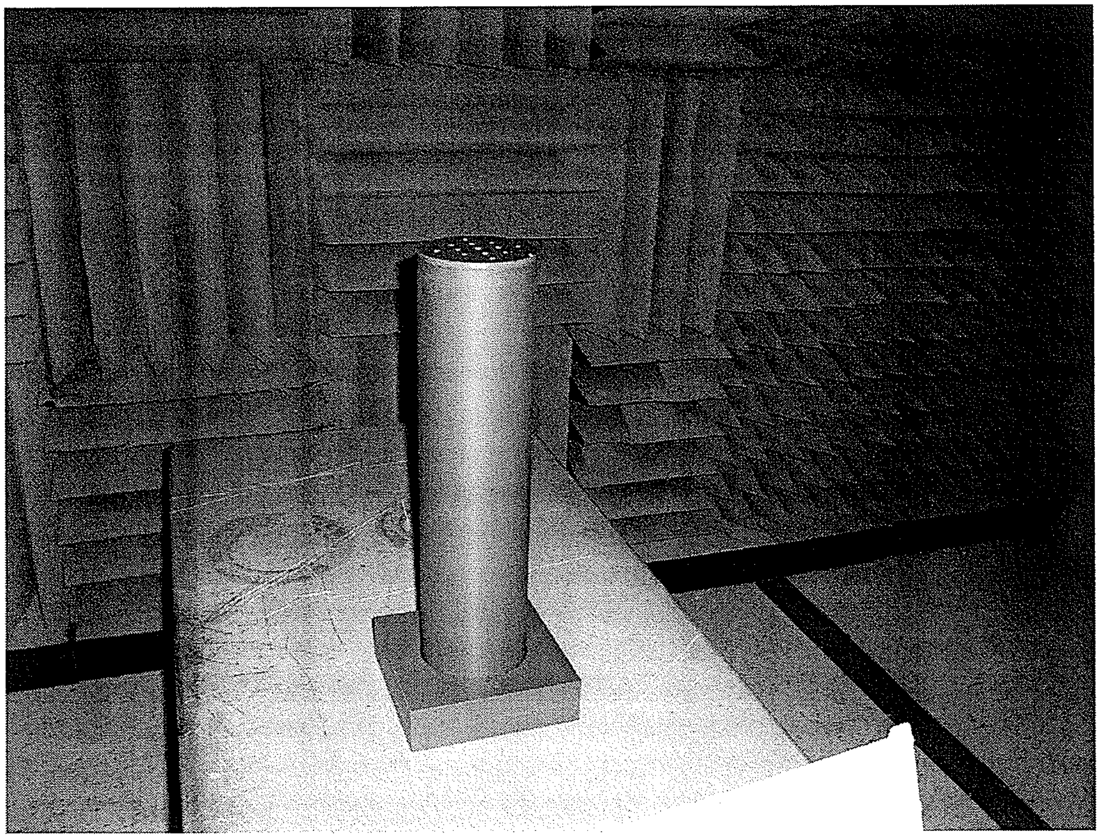

Figure 5.1. Phantom used for data acquisition along a cylindrical trajectory.

An experimental setup with two dowels and its reconstructed image are shown in figure 5.2 a) and b) respectively. The reflection of the dowels located at (2 cm,0 cm) and (-2 cm,0 cm) from the origin are however obscured by the surface reflections. In order to have a better visualization of the target signatures, the surface reflections were removed using the method proposed by the authors in [33]. This surface removal algorithm uses the Wavelet Transform (WT) to detect the singularities of the signals and is capable of performing signal decomposition at several scales [34]. This property is used to obtain the product between the scales in order to preserve the singularities of the signal that correspond to target responses and eliminate the surface. The result of the surface removal process mentioned above can be seen in figure 5.2 c). The red circle denotes the location of the removed PVC reflections. A more detailed discussion about the attenuation of the reflections from the surface is out of the scope of this thesis. Considerable work has been done in the area of removal of surface reflections, and there are currently other approaches that can be used for this purpose, such as the use of impedance coupling materials [35] or adaptive filtering [11].

A second experimental setup and its reconstructed image are shown in figure 5.3 a) and b) respectively. In this case, the surface reflections have been already removed from the reconstructed image. The dowels are located at (2 cm, 0 cm) and (0 cm, 2 cm). The separation between the dowel centers is 2.82 cm. Note that there is no overlap of the target signatures. Figure 5.4 a) shows the result of a third experimental setup when a dowel is closer to the PVC wall. The reconstructed image is shown in figure 5.4 b). The dowels are located at (2 cm, 0 cm) and (-2 cm,-2 cm) from the origin.

In order to further test the performance of the proposed method on a propagation medium different than air, a second phantom was created. This phantom consists on a pine wood trunk as the propagation medium. One aluminum rod and one plastic (E_r=2.25) rod were used as to simulate a high and low contrast target respectively. Both rods had a diameter of 3 cm. The data was acquired using a full circular trajectory with a separation of 5° between scan locations, with a radius of 0.15 m. A photograph of the phantom and a diagram experimental setup can be seen in figure 5.5 a) and b) respectively. The reconstructed data using the proposed method is shown in figure 5.5 c). The reflections of the plastic rod are obscured by the surface and the aluminum rod. Tables 5.2 and 5.3 present a quantitative summary of the previous experiments. The real and the measured positions of the target reflections are shown in Table 5.2. Table 5.3 shows the measured spread of the dowel reflections.

In order to assess the performance of the proposed method, the collected data from both phantoms was reconstructed using confocal mapping. This approach was chosen because, according to the results published in the literature, it is the one that has provided the imagery with the highest signal to noise ratios and spatial accuracy values [23]. Additionally, this is the only time-shift technique that has been tested in a multitarget environment. The results for the experimental setups shown in figures 5.2a), 5.3a) and 5.4a) can be seen in figure 5.6 a), b) and c) respectively. The result of the shift-sum reconstruction approach on the data collected from the wood trunk is shown in figure 5.6 d). Finally, the performance of the proposed method and the shift-sum technique is summarized in Table 5.4. The metrics used to assess the performance of both approaches were the signal to noise ratio and conditional entropy [36]. The SNR of the 2D images reconstructed using the proposed technique was calculated as follows:

$$SNR_{w,2D} = 20 \cdot \log_{10}\left(\frac{\sum_{q=1}^{T} \Gamma_{q,3dB}^{2D} / T}{\sigma^{w}} \right) \tag{5.1}$$

where $\Gamma_{p,3dB}^{2D}$ is the magnitude of the 3dB point of the p^{th} target signature in the 2D model generated by the proposed algorithm and σ^{w} is the standard deviation of the background noise. Due to the fact that the output of the confocal mapping approach is the energy of the reconstructed model, the SNR for the 2D images reconstructed using this focusing technique is given by:

$$SNR_{c,2D} = 10 \cdot \log_{10}\left(\frac{\sum_{q=1}^{T} \Gamma_{q,3dB}^{c,2D} / T}{\sigma^{c}} \right) \tag{5.2}$$

where $\Gamma_{p,3dB}^{c,2D}$ is the magnitude of the 3dB point of the p^{th} target signature in the 2D model produced by the confocal mapping approach and σ^{c} is the standard deviation of the background noise.

In an image processing context, conditional entropy is defined as the entropy on a determined set of intensity values on the image. As discussed in [37], the entropy of an image is the uncertainty on the pixel intensity values in the image that is directly related to the level of spread on its histogram. In digital images, the conditional entropy can be defined as:

$$H(\eta) = -\sum_{W} p(w_d) \sum_{\eta_{\max}} p(\eta \mid w_d) \log_2 p(\eta \mid w_d) \tag{5.3}$$

where W is the total number the data clusters on the image and $p(\eta \mid w_d)$ is the probability density function of the η pixel intensity value in the d^{th} data cluster, $\eta \in [1, \eta_{\max}]$, and $\eta_{\max}$ is the total number of pixel intensity values in the image. If the attention is centered in the q^{th} cluster, its entropy is equal to:

$$H(\eta \mid w_d = w_q) = -\sum_{\eta_{\max}} p(\eta \mid w_d) \log_2 p(\eta \mid w_d). \tag{5.4}$$

As the spread on the different data clusters in the image become smaller, the focus quality increases. Conditional entropy is useful in situations where the amount of pixels affected by the focusing process is small compared to the total number of pixels on the image.

The average execution time of the proposed method was 12.5 sec. The confocal mapping presented a 2.5 sec execution time. Although the computational cost of the proposed method is higher than confocal mapping, it still has an execution time in the order of seconds.

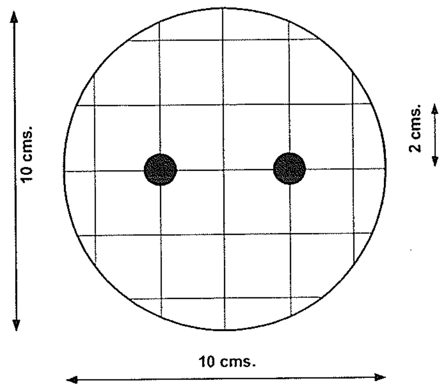

a)

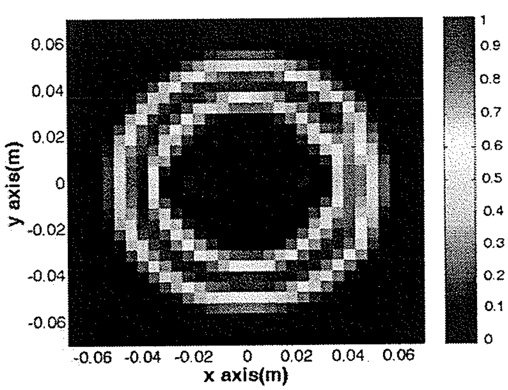

b)

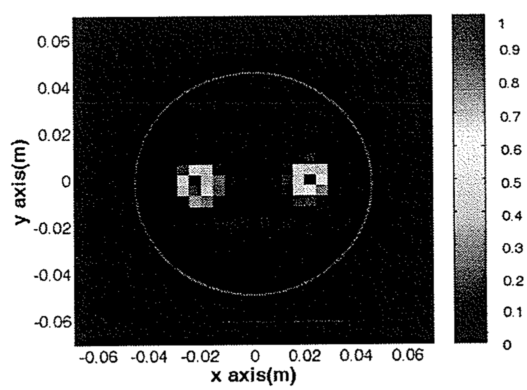

c)

Figure 5.2. a) Experiment 1 setup. b) Reconstructed image. c) Reconstructed image after the surface removal process.

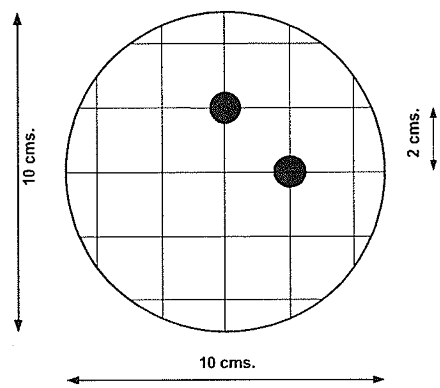

a)

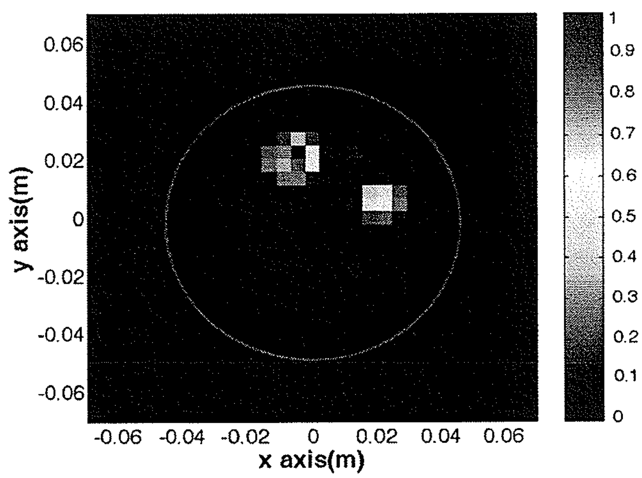

b)

Figure 5.3. a) Experiment 2 setup. b) Reconstructed image.

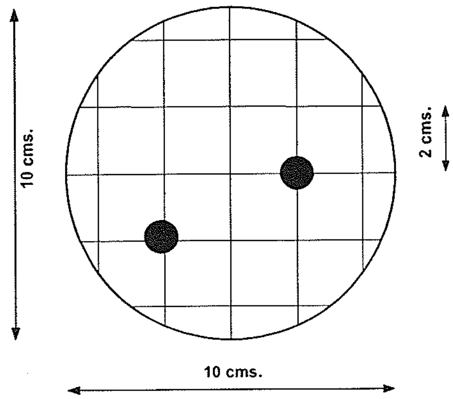

a)

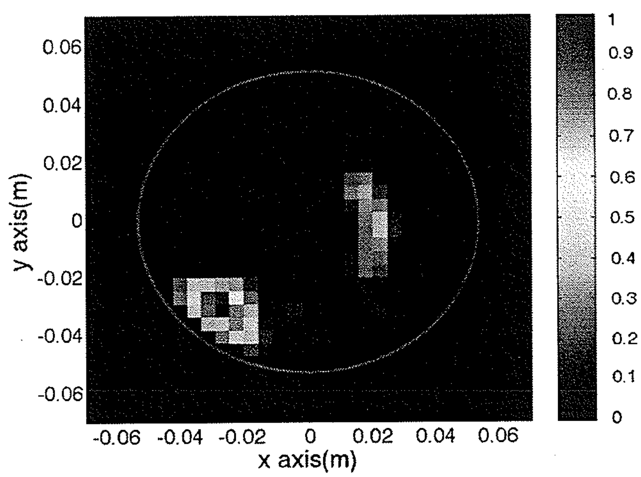

b)

Figure 5.4. a) Experiment 3 setup. b) Reconstructed image.

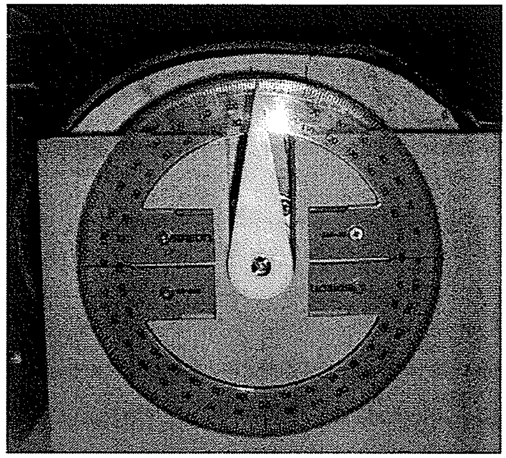

a)

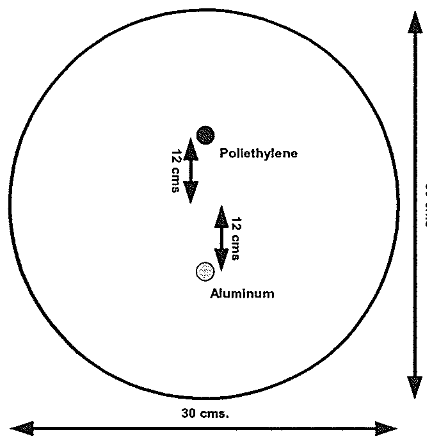

b)

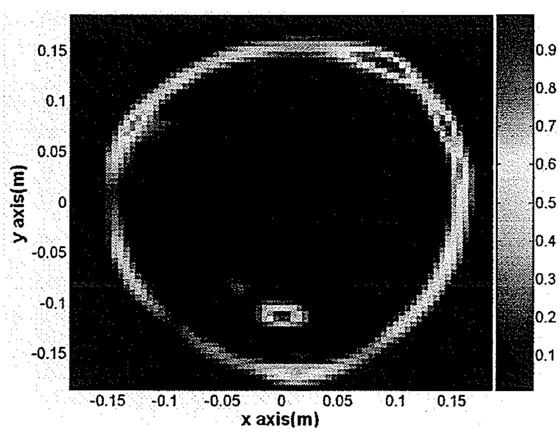

c)

Figure 5.5. a) Wood trunk phantom. b) Experiment 4 setup. c) Reconstructed image.

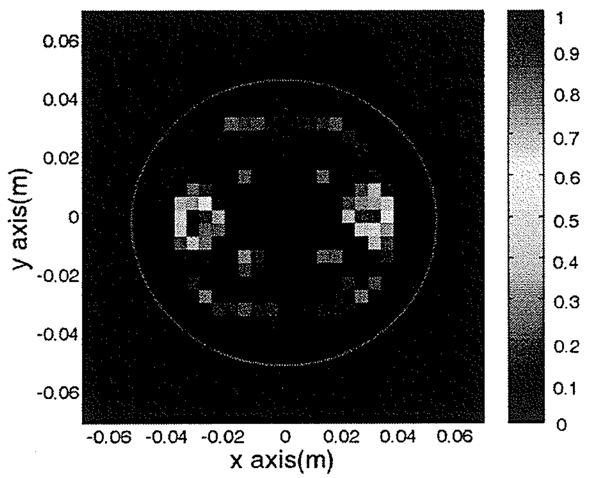

a)

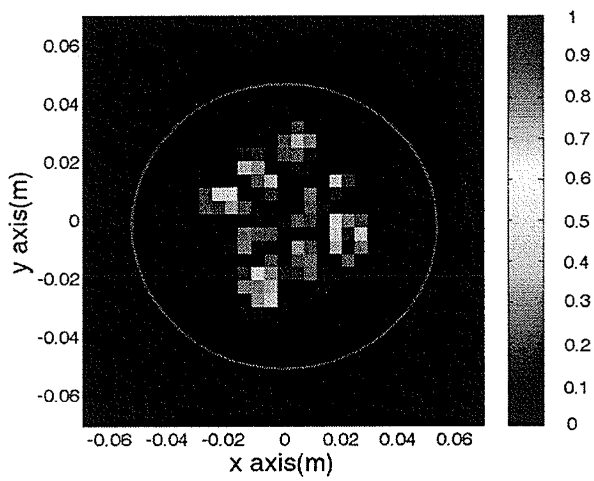

b)

Figure 5.6. Shift sum reconstructed images from: a) Experiment 1 data. b) Experiment 2 data.

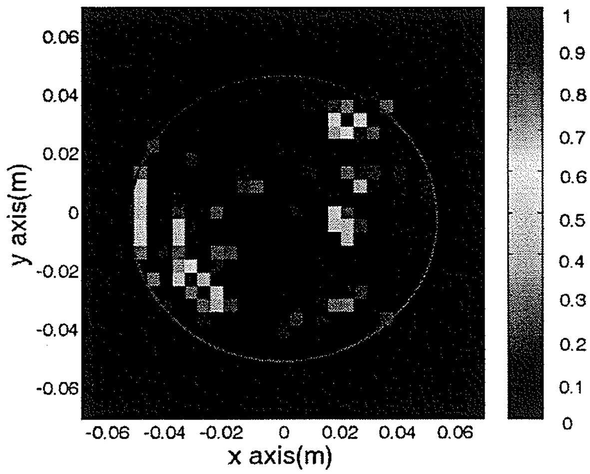

c)

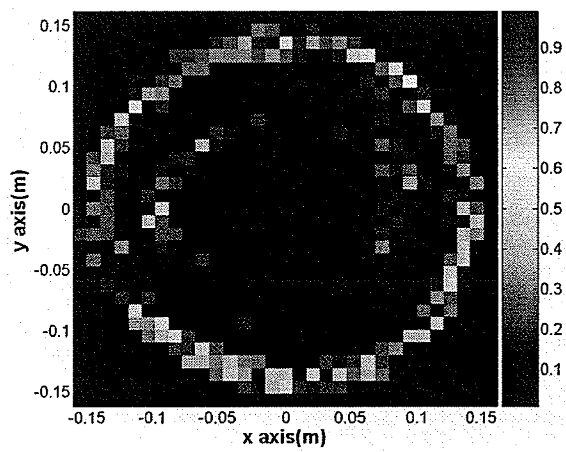

d)

Figure 5.6. Shift sum reconstructed images from: c) Experiment 3. d) Experiment 4 data.

TABLE 5.2

Errors in the target signature locations in each 2D experiment

Target	Reconstructed location, cm	Error, cm
1a	-2.20,0.0	-0.20,0.0
2a	2.20,0.0	0.20,0.0
2b	-0.20,2.20	-0.20,0.2
3a	2.20,0.20	0.20,0.20
3b	-2.30,-2.40	0.30,0.40
4a	0.60,-12.24	0.60,-0.24

TABLE 5.3

Target sizes and dimension errors for each 2D experiment

Target	Reconstructed size, cm^2	Error, cm^2
1a	1.65	-0.10
2a	1.86	0.10
2b	1.45	-0.30
3a	1.65	-0.10
3b	1.65	1.30
4a	7.86	0.79

TABLE 5.4

SNR and Conditional Entropy values comparison in each 2D experiment

Exp.	$SNR_{w,2D}$ (dB)	$SNR_{c,2D}$ (dB)	Wavefront Cond. Entropy(bits)	Shift-Sum Cond. Entropy (bits)
1	10.65	5.47	3.45	3.52
2	9.14	0.66	3.16	3.80
3	9.00	2.57	3.16	3.58
4	11.81	3.32	5.00	5.80

5.3 3D data acquisition system description

In order to test the proposed 3D reconstruction method, the same network analyzer (Wiltron 360B) and antenna (AEL H horn) were used. In this case, the antenna was mounted on a support base that is mechanically attached to a geared mechanism that allows vertical motion. This mechanism is operated by a stepper motor (Princess Auto Inc. model 0756676). The mechanism support base is made of wood and surrounded by electromagnetic waves absorbing materials. The phantom is mounted into a platform made of maple wood with a height of 25 cm. In order to accurately emulate a cylindrical scan trajectory, the platform is attached to the top of a step motor (Atlanta Scientific Inc. model 56060) in order to rotate the phantom. Both step motors are controlled using a custom designed electronic system. This control system can communicate to a PC via the serial port in order to specify the desired scan locations. A bandwidth of 11 GHz (1-12 GHz) was used in all the experiments. The system radiated the same waveform than the one used in the 2D experiments. Also, the data acquisition setup was calibrated using the same protocol than the one used for the 2D data acquisition system. The data was reconstructed using a 3 GHz PC with 2 GB RAM.

5.4 Cylindrical experiments

For cylindrical scans, a phantom similar to the one used in the previous circular experiments was employed. This phantom consisted of a PVC pipe filled with foam disks. The PVC pipe has an inner diameter of 10 cm and a height of 90 cm. Aluminum ovoids were used as targets. The ovoids have a 1.2 cm diameter and a 3 cm height. The phantom materials present almost no variation in their dielectric permittivity values in the 1-12 GHz frequency range. The dielectric permittivity values of the materials used in the support base and the phantom structure are shown in Table 5.5. A diagram and a photograph of the data acquisition setup can be seen in figure 5.7 a) and b) respectively.

The data acquisition process was performed by rotating the phantom at 5° intervals for a total of 72 positions. At each position, the collected reflections were recorded. In order to allow the beamwidth to illuminate the entire phantom and reduce undesirable interferences of antenna early time artifacts, the distance between the antenna and the center of the phantom was set to 70 cm. Along the z axis, the data was acquired at 15 scan planes with a separation of 1 cm. For the Fourier processing of the collected data, a zero padding factor of 2 was used to improve the visualization of the reconstructed images. The zero padding factor in this set of experiments was reduced as a result of the increase of memory requirements due to the additional scan planes. In the following discussion, the center of the phantom will be denoted as the origin, and the displayed images show the normalized energy of the reconstructed data.

TABLE 5.5

Permittivity values of the materials used in the phantom structure and support base

Material	**Permittivity Value (E_r) at6 GHz**
PVC	3
Air	1
Maple wood	1.55
Synthetic foam	1.05

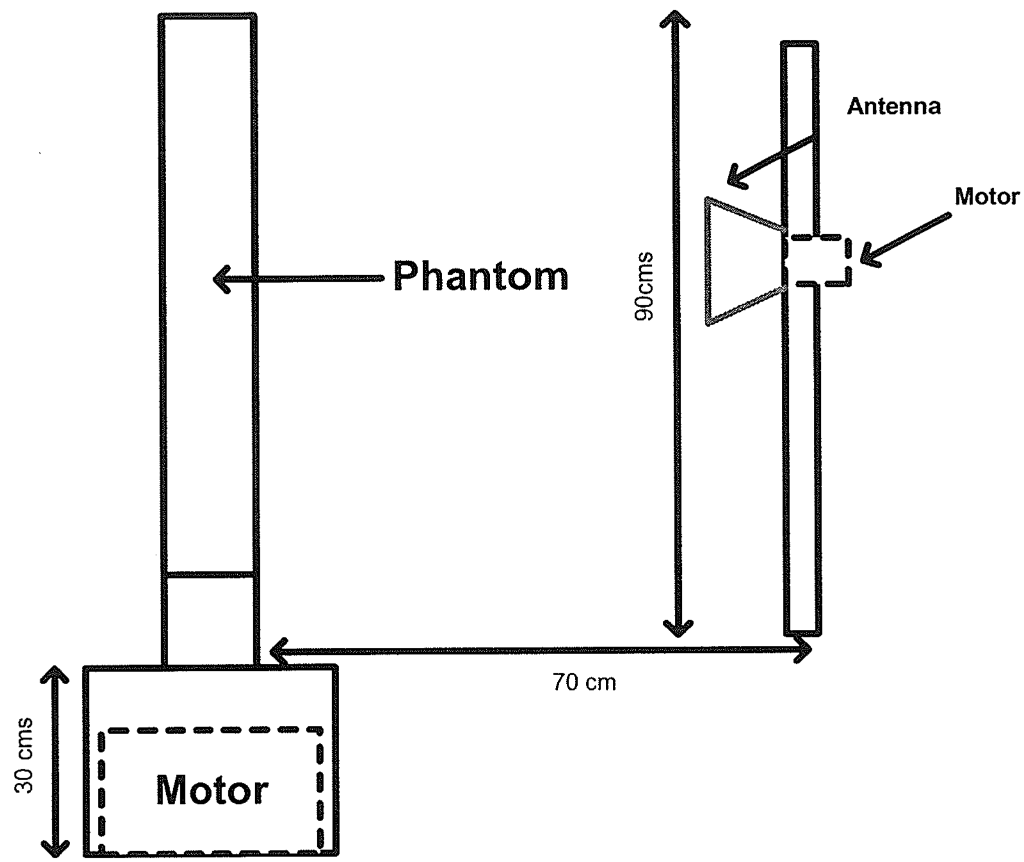

a)

Figure 5.7 a) Diagram of the data acquisition system.

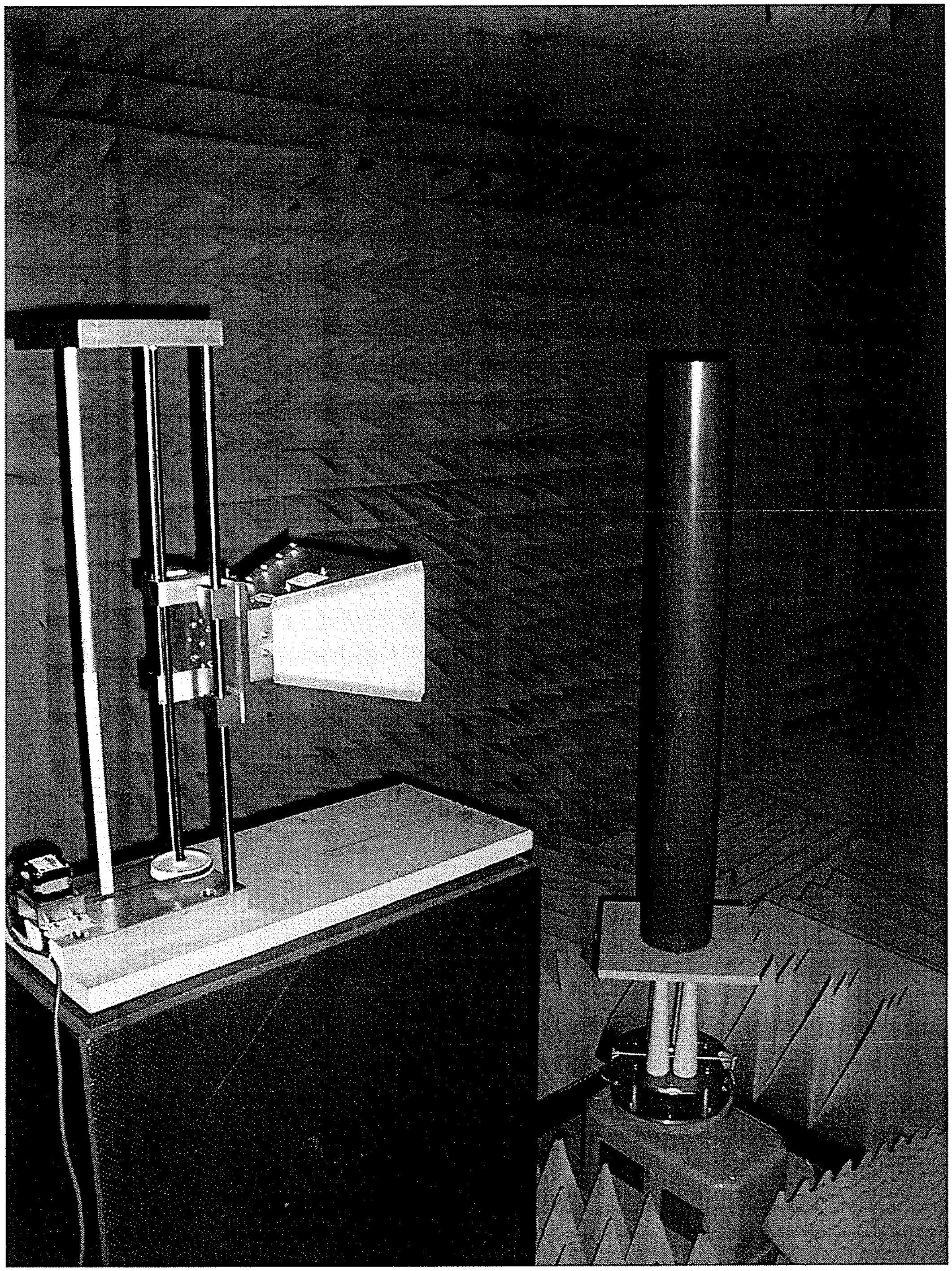

b)

Figure 5.7. b) Photograph of the data acquisition setup.

A 3D experimental setup with one target and its reconstructed image are shown in figure 5.8 and 5.9 respectively. This experiment will be referred as experiment 5. Similarly to the circular scan trajectory results, the normalized energy of the reconstructed data is displayed. In this experiment, a single ovoid was positioned at (-0.5 cm,-02.2 cm, 2.5 cm) from the origin. As it can be seen, the highest intensity clutter in the image is due to surface reflections. In order to have a better visualization of the target signatures, the surface can be removed using the method proposed in [33]. The result of the surface removal process can be seen in figure 5.9 b).

A second 3D experimental setup, denoted as experiment 6, and its reconstructed image are shown in figure 5.10 and 5.11 respectively. In this case, the surface reflection has been already removed from the reconstructed image. Two targets were used in this experiment. The ovoids were positioned at (-2 cm, 0.65 cm, 3.5 cm) and (2.6 cm, 0 cm, 3.5 cm). As it can be seen in figure 5.10 and 5.11, there is no overlap between the target signatures. A third 3D experimental setup, which we will refer as experiment 7, and its corresponding model are shown in figure 5.12 and 5.13. In this experiment, the targets are positioned at (2.6 cm,0 cm,4.5 cm) and (0 cm,2.6 cm,-1.5 cm).

In order to assess quantitatively the performance of the proposed method, the locations and size differences between the real target dimensions and the reconstructed target reflections were measured. The errors between the real and the reconstructed target locations can be seen in Table 5.6. The dimension and size errors of the target signatures in each experiment are shown in Table 5.7. In addition, the data collected in each experiment was reconstructed using the 3D version of the confocal mapping approach [38, 39]. The resulting models corresponding to the experimental setups shown in figures

5.9, 5.11 and 5.13 can be seen in figure 5.14 a), b), c) and d). The metric used to quantitatively assess the performance of each technique was the SNR. The SNR of the 3D models reconstructed using the proposed technique was calculated as follows:

$$SNR_{w,3D} = 20 \cdot \log_{10}\left(\frac{\sum_{q=1}^{T} \Gamma_{q,3dB}^{3D} / T}{\sigma^{w}} \right) \tag{5.5}$$

where $\Gamma_{q,3dB}^{3D}$ is the magnitude of the 3dB point of the p^{th} target signature in the 3D model generated by the proposed algorithm and σ^{w} is the standard deviation of the background noise. Due to the fact that the output of the confocal mapping approach is the energy of the reconstructed model, the SNR for the 3D images reconstructed using this focusing method is given by:

$$SNR_{c,3D} = 10 \cdot \log_{10}\left(\frac{\sum_{q=1}^{T} \Gamma_{q,3dB}^{c,3D} / T}{\sigma^{c}} \right) \tag{5.6}$$

where $\Gamma_{q,3dB}^{c,3D}$ is the magnitude of the 3dB point of the p^{th} target signature in the 3D model produced by the confocal mapping approach and σ^{c} is the standard deviation of the background noise. The calculated $SNR_{c,3D}$ and $SNR_{w,3D}$ values for each data set are summarized in Table 5.8.

Finally, the computational cost of the proposed technique was evaluated by calculating the average execution time of 90 simulations. The number of scan locations in each plane varied between 72 and 200, and the number of scan planes ranged between 10 and 21. The average execution time needed to focus each plane was 40.5 sec.

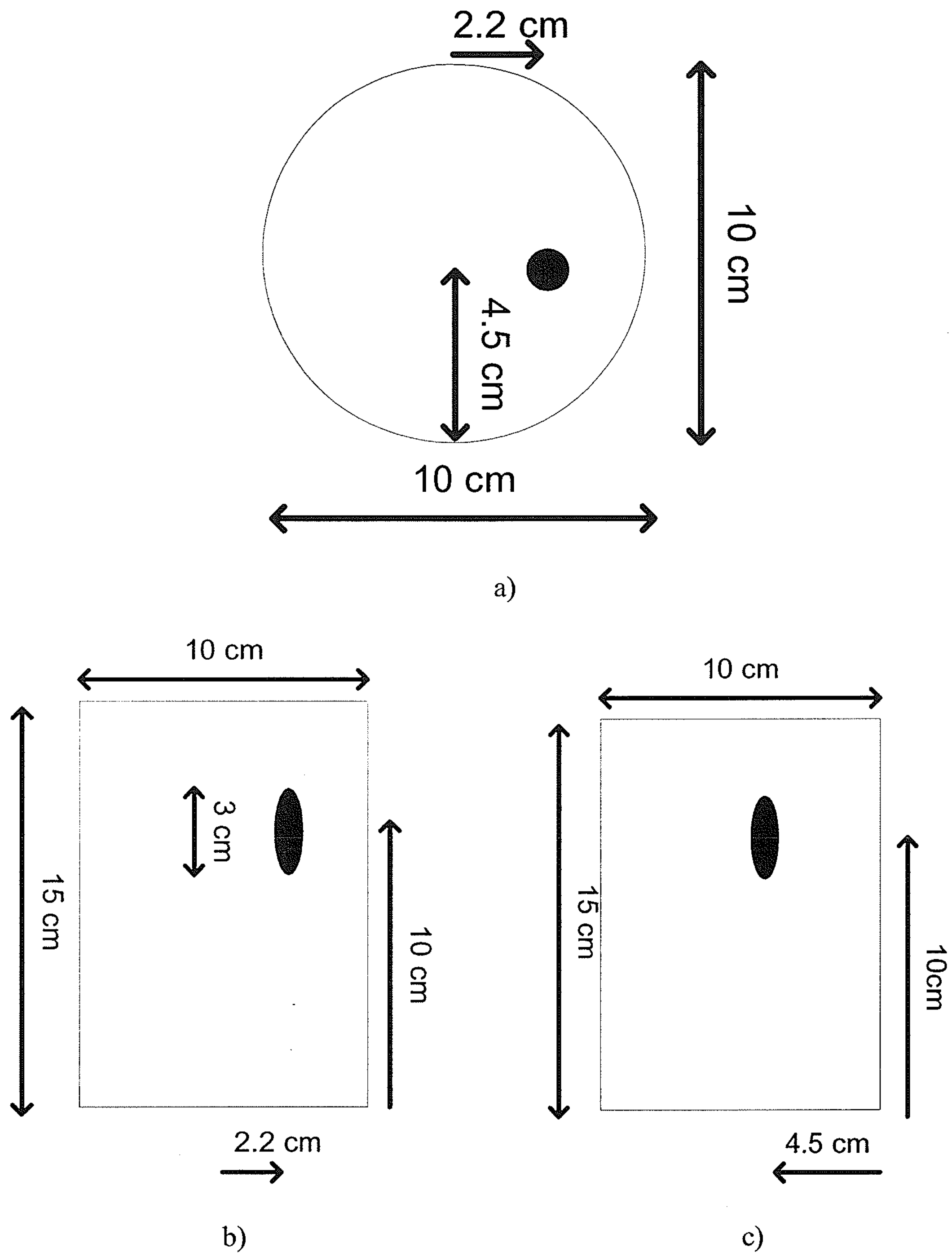

Figure 5.8. Experiment 5 setup. a) Axial view. b) Coronal view. c) Sagital view.

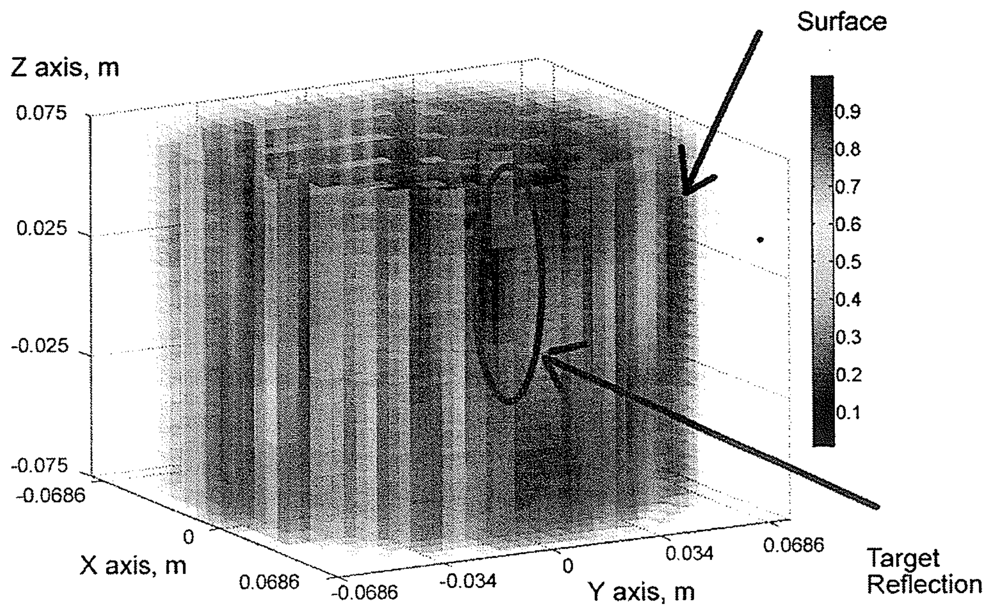

a)

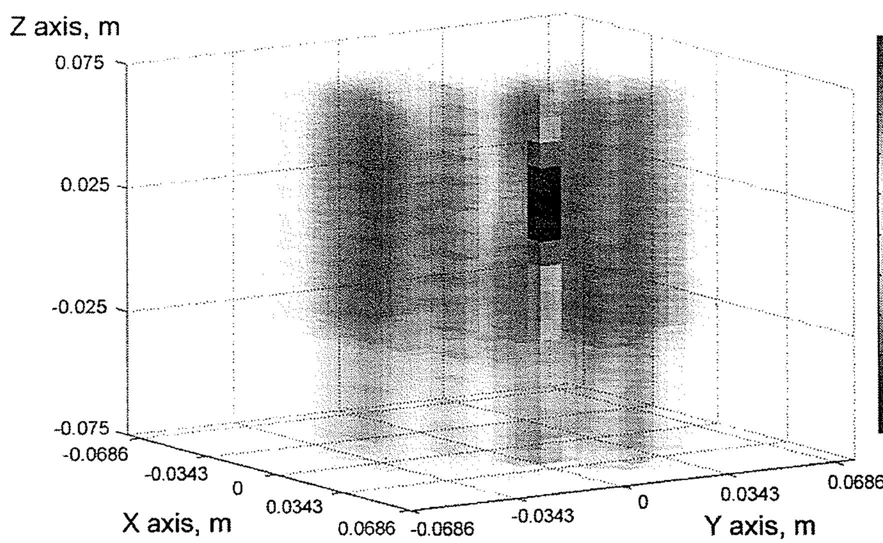

b)

Figure 5.9. Experiment 5 reconstructed image. a) 3D model with surface clutter present. b) 3D model produced after the surface clutter removal.

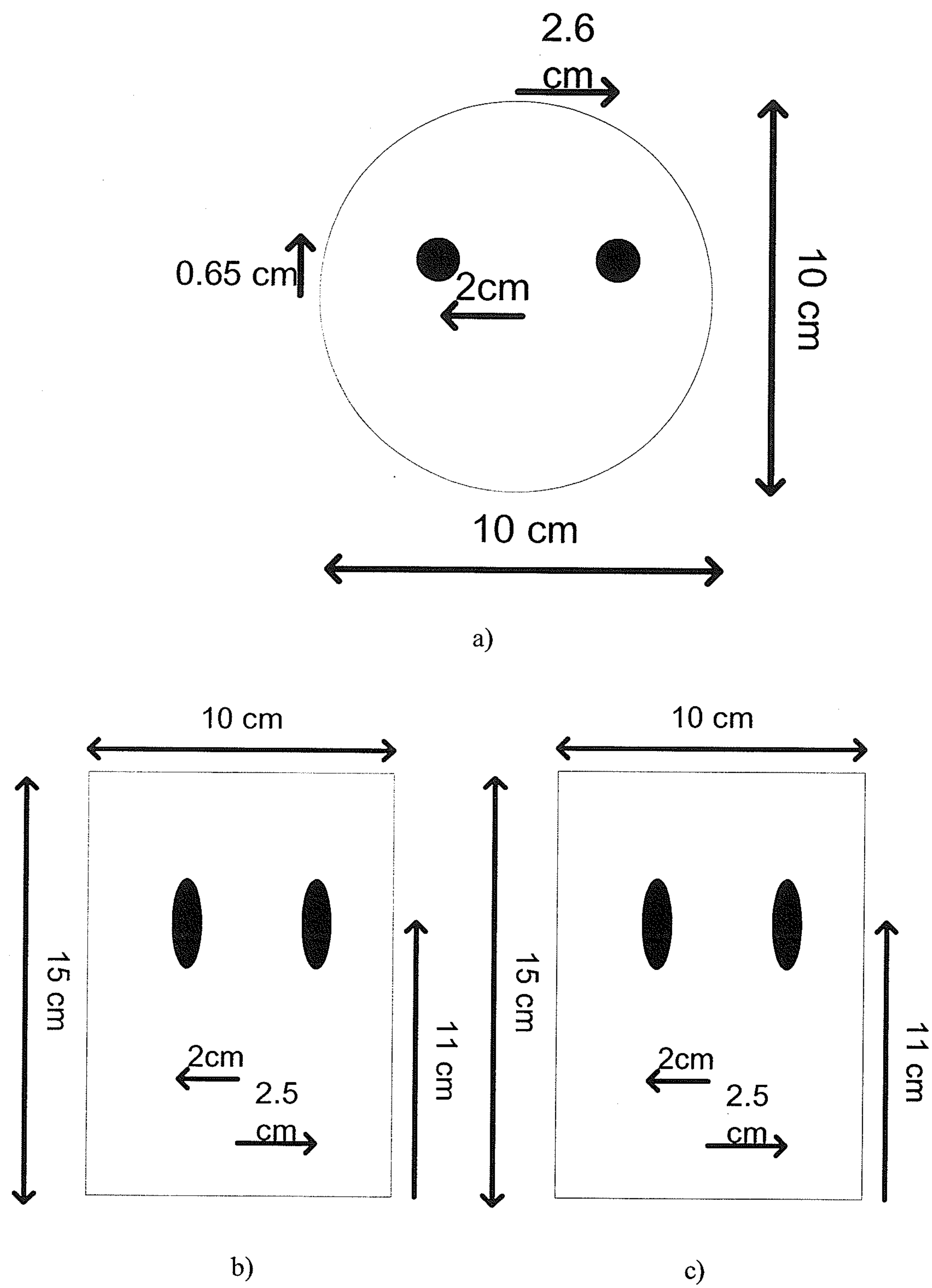

Figure 5.10. Experiment 6 setup. a) Axial view. b) Coronal view. c) Sagital view.

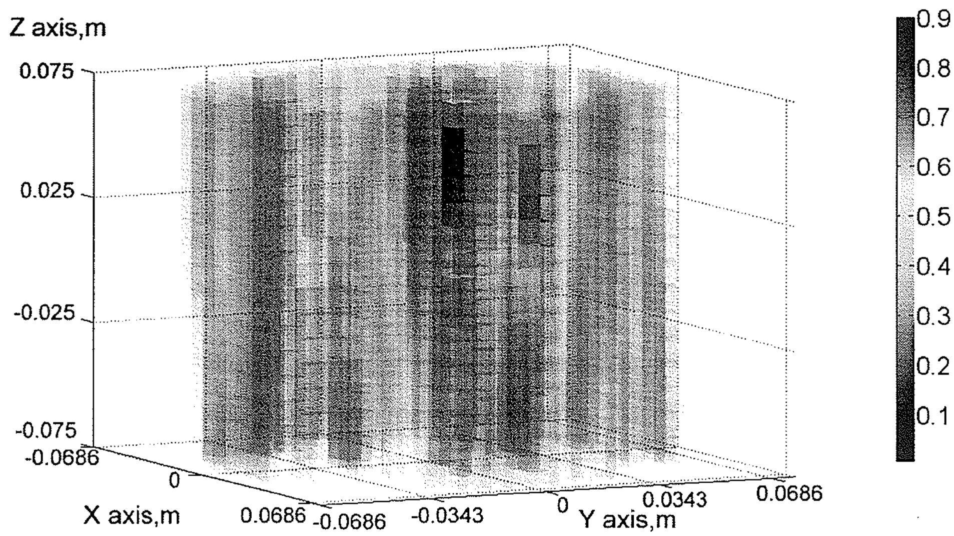

a)

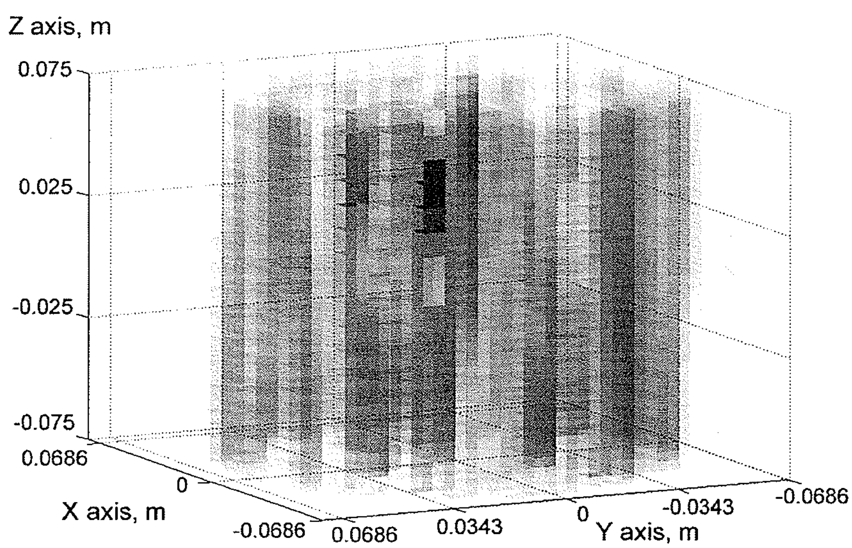

b)

Figure 5.11. Experiment 6 reconstructed image. a) Close up on the first target. b) Close up on the second target.

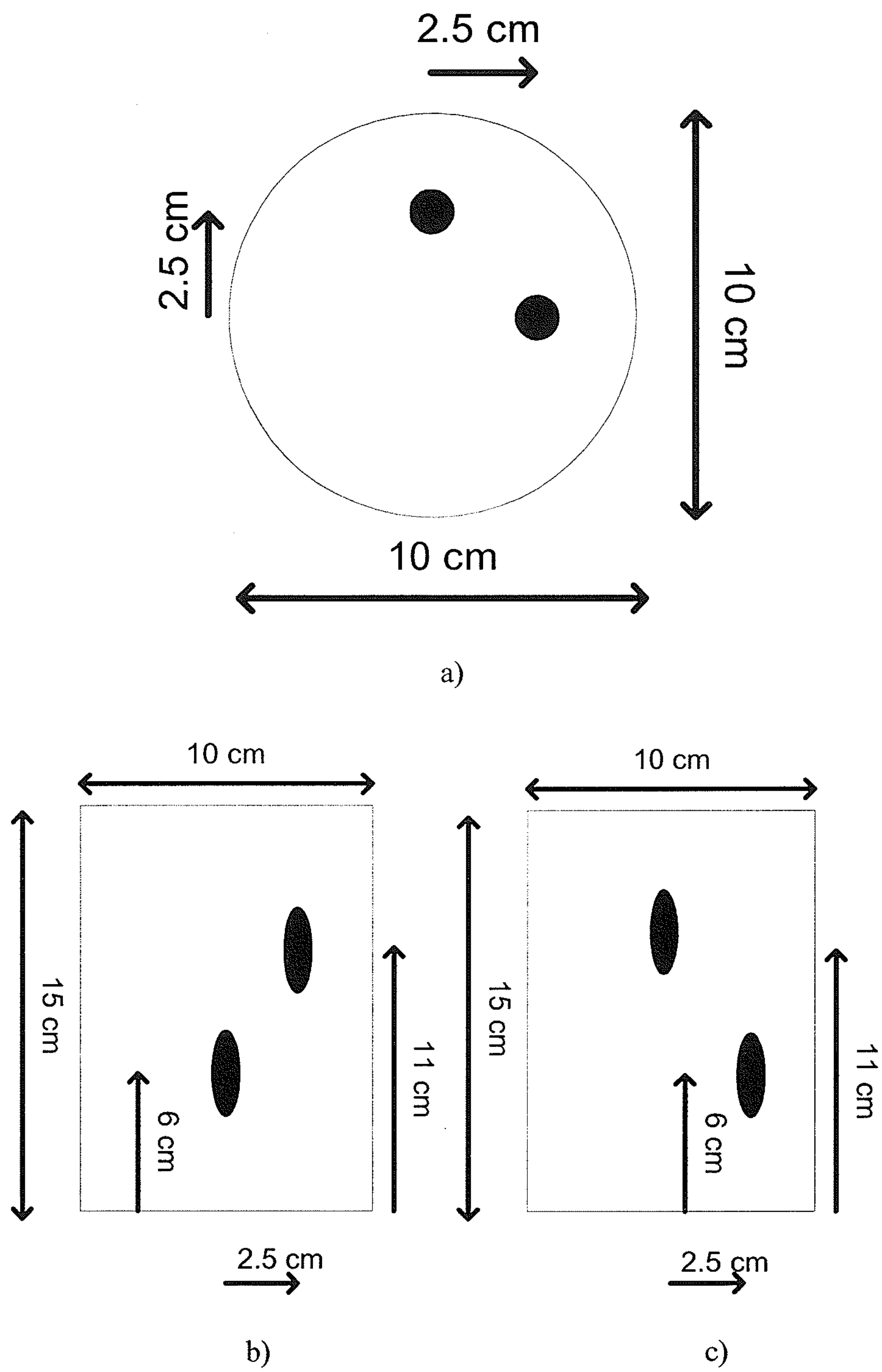

Figure 5.12. Experiment 7 setup. a) Axial view. b) Coronal view. c) Sagital view.

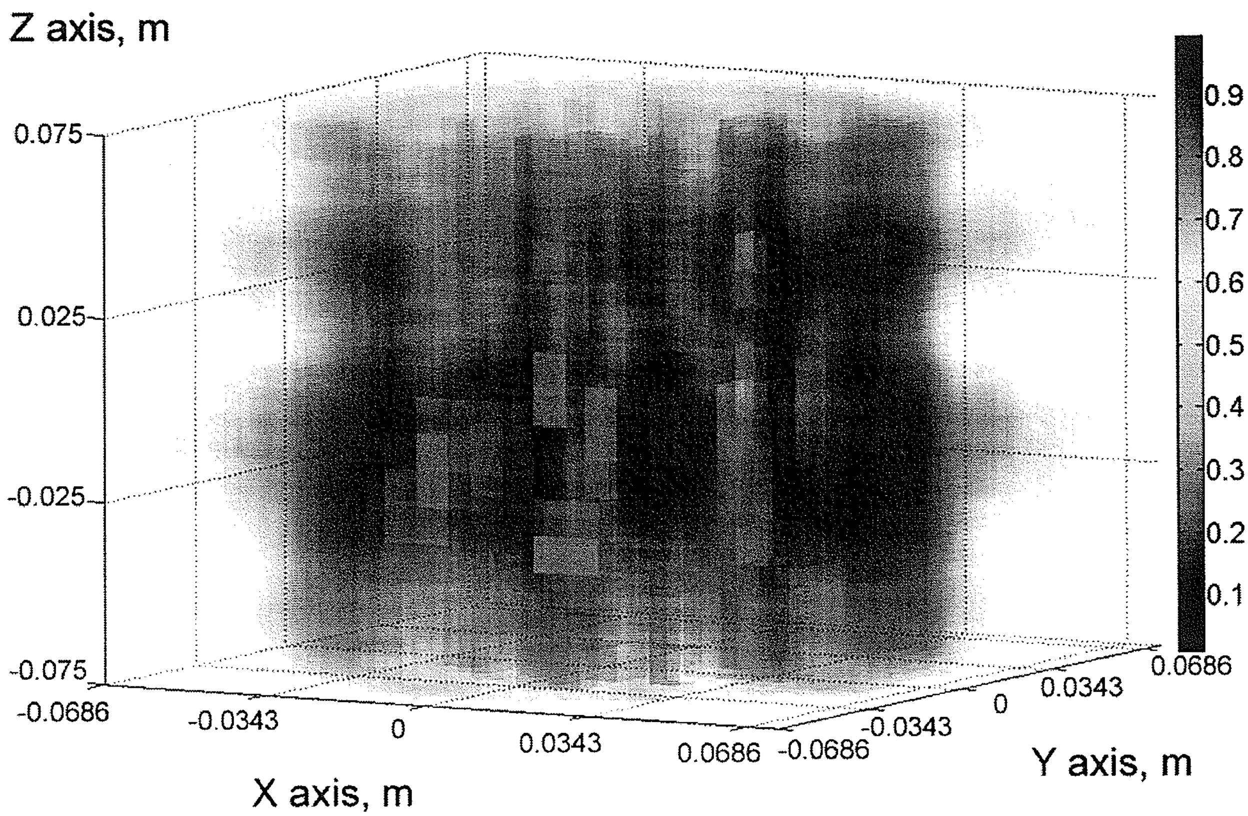

Figure 5.13. Experiment 7 reconstructed image.

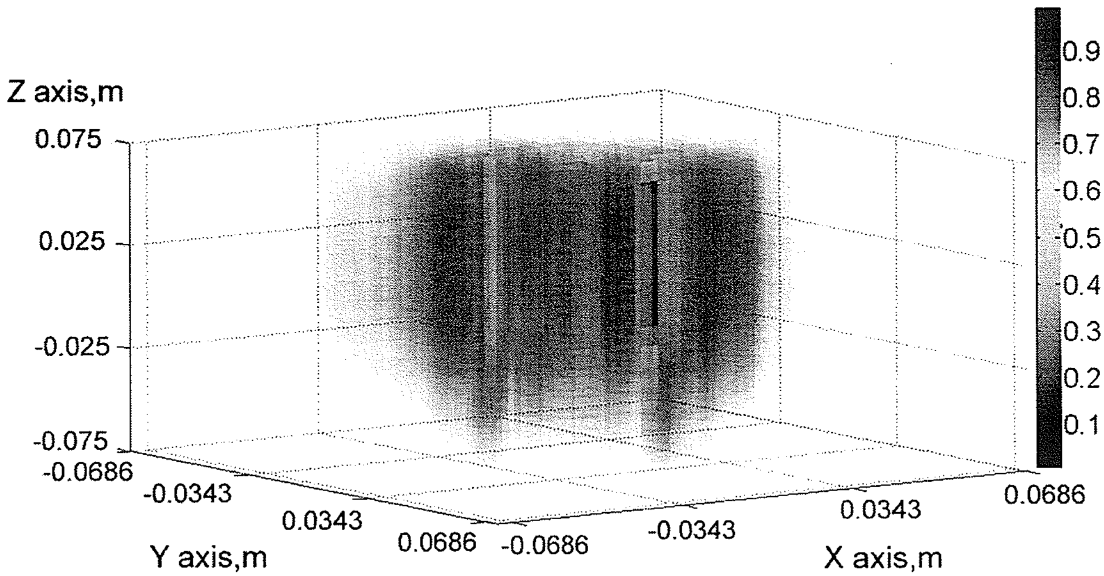

(a)

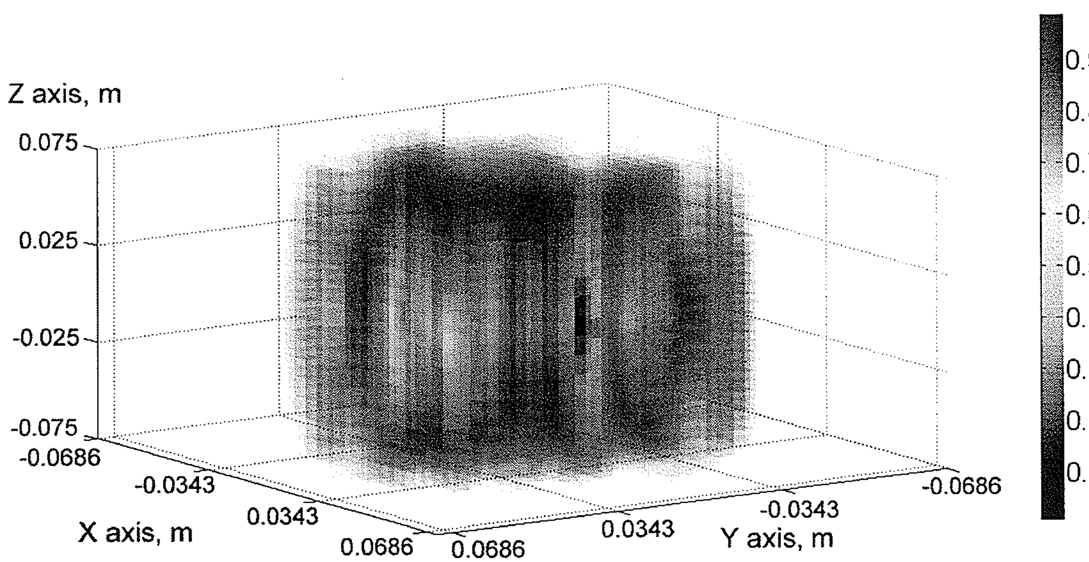

(b)

Figure 5.14. Cylindrical experimental data sets reconstructed using the confocal mapping approach. a) Reconstructed model from the data collected in experiment 5. b) Reconstructed model from the data collected in experiment 6. Close up on the first target.

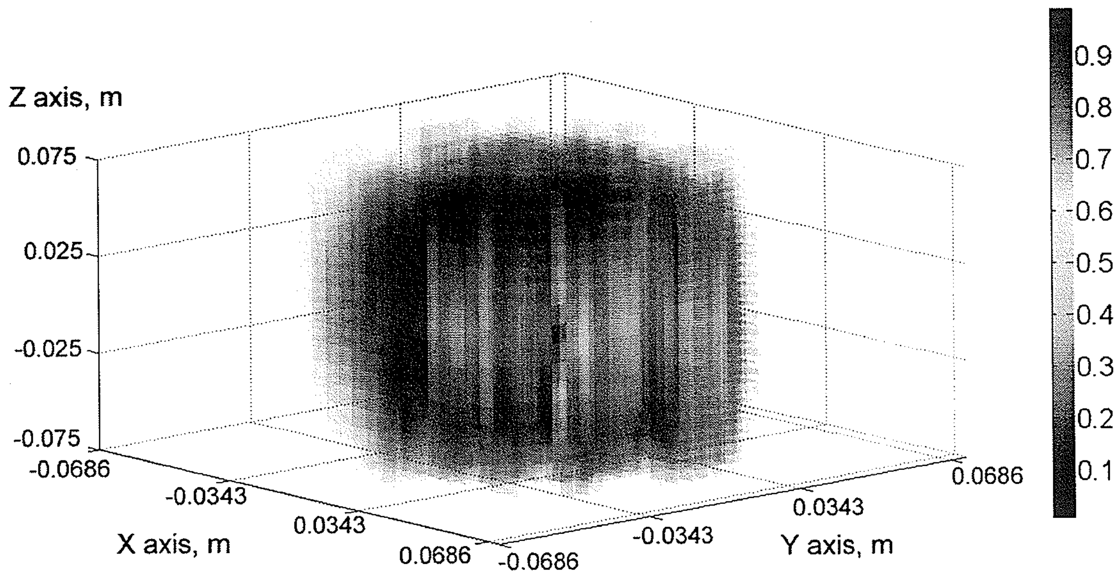

(c)

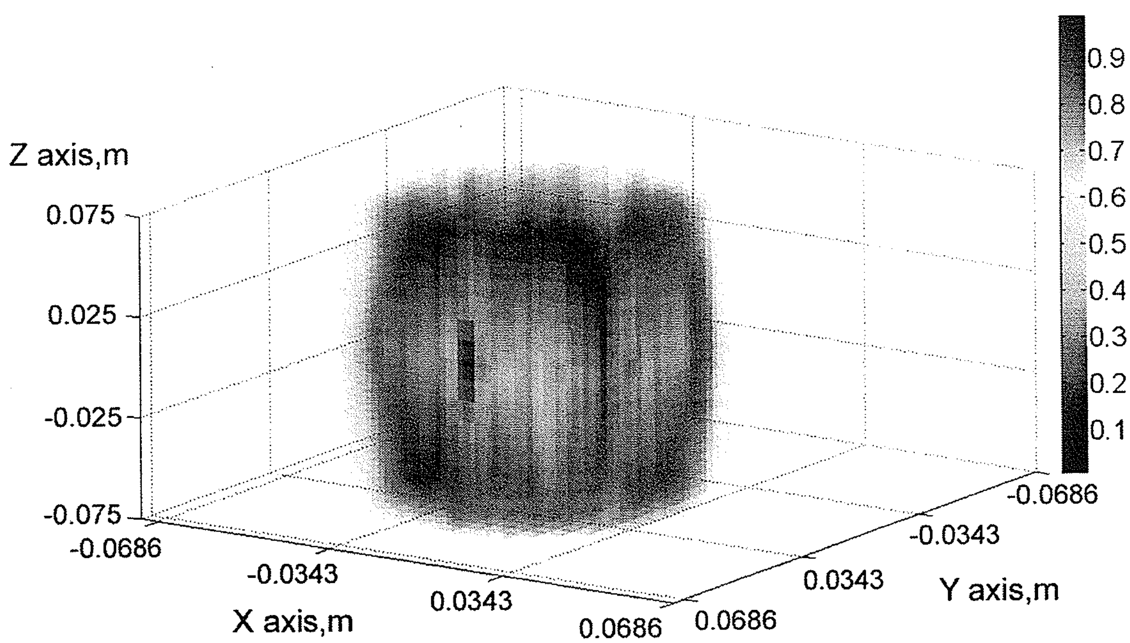

(d)

Figure 5.14. Cylindrical experimental data sets reconstructed using the confocal mapping approach. c) Reconstructed model from the data collected in experiment 6. Close up on the second target. d) Reconstructed model from the data collected in experiment 7.

TABLE 5.6

Errors in the target signature locations in each 3D experiment

Target	Reconstructed Location, cm	Error, cm
5a	-0.68,-2.04,2.50	0.18,0.2,0
6a	2.72,0.68, 3.50	0.12,0.03,0
6b	-2.1,0.68, 3.50	-0.1,0.03,0
7a	2.72,0,4.50	0.12,0,0
7b	0, 2.72,-2.00	0,0.12,-0.50

TABLE 5.7

Dimensions and size errors of the target signatures in each 3D experiment

Target	Size, cm^3	Error, cm^3
5a	2.77	-0.61
6a	2.77	-0.61
6b	3.23	-0.16
7a	2.77	-0.61
7b	2.31	-1.08

TABLE 5.8

SNR and Conditional Entropy values comparison in each 3D experiment

Exp.	$SNR_{w,3D}$ (dB)	$SNR_{c,3D}$ (dB)	Wavefront Cond. Entropy(bits)	Shift-Sum Cond. Entropy (bits)
5	8.77	2.94	3.66	5.58
6	8.48	3.36	4.55	5.05
7	6.45	2.93	4.36	5.25

6. CONCLUSIONS

In this thesis, two wavefront reconstruction methods for SR data acquired along circular and cylindrical scan geometries are proposed. The algorithms are based on processing the phase variations exhibited by target reflections along the slow-time trajectories. These differences are used to migrate the target responses from the spatial temporal domain where they are originally collected to a Cartesian space where they are to be displayed. The proposed approaches consist of a match filtering operation and a series of remapping processes performed in the frequency domain. The spectrum of the spf was calculated along the slow-time directions using the stationary phase method. This mathematical approach was chosen because it produces a close form expression. The majority of the mathematical work shown in this thesis, with the exception of the proof shown in the appendix I, was developed by the author.

Theoretical aspects, such as the size of the psf and sampling constraints, were described and illustrated. This analysis was performed by determining the support band of the spf spectrum. In order to determine the experimental feasibility of the proposed method an experimental data acquisition system was assembled. This system was used to record experimental data sets from phantoms that mimic the dielectric properties present in different SR scenarios. The proposed methods produced spatial accurate imagery with acceptable SNR values at reasonable computational cost. In order to compare the performance of the proposed algorithms with the current circular and cylindrical SR reconstructions approaches, the experimental data sets were reconstructed using the 2D and 3D versions of the confocal mapping algorithm. The proposed methods produced better quality imagery with a higher SNR, at a slower execution time which nevertheless is still in the order of seconds. Furthermore, the proposed approach has a number of advantages over the confocal mapping algorithm. First, it uses takes advantage of the radar-doppler effect to transfer the collected target responses to their original spatial locations. This is the main reason why the proposed methods do not yield artifacts in their reconstructed imagery. Secondly, the proposed method does not require a characterization of the antennas. Finally, no focal regions must be defined in the scan area.

Future research will be concentrated on three main aspects. First, the proposed techniques will be tested on experimental data sets collected from more complex phantoms in order to evaluate their feasibility on more realistic scenarios. Another area of interest is the reduction of the computational cost of the proposed algorithms. Finally, the signal model used by the proposed methods can also be used for other echo based imaging techniques, such as ultrasound. Further work will be done to evaluate the feasibility of the proposed algorithms in ultrasound imaging.

APPENDIX I

Consider the general case of (2.5):

$$E(k)=\int_{v_s}^{v_f} f(t)\exp(jk\mu(t))dt \tag{A1.1}$$

Assuming that the interval (v_s,v_f) is finite, from the integrability of $f(t)$, we can find a sufficiently fine subdivision of (v_s,v_f) such that if:

$$e_l=\min f(t) \quad \text{for } t_l \le t \le t_{l+1} \tag{A1.2}$$

then for any k, the integral:

$$E_q(k)=\sum_{l=0}^{q-1}\int_{t_l}^{t_{l+1}} e_l\cdot\exp(jk\mu(t))dt \tag{A1.3}$$

differs from $E(k)$ by less that ι, where ι is a given number greater than 0. This can be expressed as:

$$\left|E(k)-E_q(k)\right|<\iota \tag{A1.4}$$

But

$$\int_{t_l}^{t_{l+1}} e_l \exp\big(jk\mu(t)\big)dt = e_l \frac{\exp\big(jkt_{l+1}\big) - \exp\big(jkt_l\big)}{jk} \tag{A1.5}$$

Hence

$$E_q(k) = \sum_{l=0}^{q-1} \left| e_l \frac{\exp\big(jkt_{i+1}\big) - \exp\big(jkt_i\big)}{jk} \right| \leq \frac{2}{k} \sum_{l=0}^{q-1} |e_l| \underset{k\to\infty}{\longrightarrow} 0\,. \tag{A1.6}$$

Therefore $E(k) = \int_a^b f(t) \exp\big(jk\mu(t)\big)dt \to 0$ when $k \to \infty$

APPENDIX II

As mentioned in [25], $\left(\lambda^*, w^*\right)$ is considered a valid stationary point of the spf $\exp(j \cdot k \cdot \mu(\lambda, w))$ if the two following conditions are satisfied:

$$\left.\frac{\partial(\mu(\lambda, w))}{\partial \lambda}\right|_{(\lambda=\lambda^*, w=w^*)} = 0 \qquad \text{(A2.1)}$$

$$\left.\frac{\partial(\mu(\lambda, w))}{\partial w}\right|_{(\lambda=\lambda^*, w=w^*)} = 0. \qquad \text{(A2.2)}$$

In order to validate the use of (θ^*, z^*) as a valid stationary point for the spf described in (3.4), the conditions expressed in (A2.1) and (A2.2) must be evaluated. First, the condition described in (A2.1) will be evaluated. As stated in chapter 3:

$$\frac{\partial\left(-2k \cdot L_p(\theta, z) + \varepsilon\theta + k_z z\right)}{\partial z} = \frac{2k(z_p - z)}{\sqrt{R^2 + r_p^{\,2} + (z_p - z)^2 - 2 \cdot R \cdot r_p \cos(\phi_p - \theta)}} - k_z. \qquad \text{(A2.3)}$$

By evaluating (A2.3) at (θ^*, z^*), the result can be expressed as:

$$\left.\frac{\partial\left(-2k\cdot L_p(\theta,z)+\varepsilon\theta+k_z z\right)}{\partial z}\right|_{(\theta=\theta^*,z=z^*)}=\frac{2k\left(z_p-z_p-\frac{k_z}{\sqrt{4k^2-k_z^2}}\sqrt{R^2+r_p^{\,2}-2\cdot R\cdot r_p\cos(\phi_p-\theta^*)}\right)}{\sqrt{R^2+r_p^{\,2}+\left(z_p-z_p-\frac{k_z}{\sqrt{4k^2-k_z^2}}\sqrt{R^2+r_p^{\,2}-2\cdot R\cdot r_p\cos(\phi_p-\theta^*)}\right)^2-2\cdot R\cdot r_p\cos(\phi_p-\theta^*)}}-k_z \tag{A2.4}$$

$$\left.\frac{\partial\left(-2k\cdot L_p(\theta,z)+\varepsilon\theta+k_z z\right)}{\partial z}\right|_{(\theta=\theta^*,z=z^*)}=\frac{2k\left(\frac{k_z}{\sqrt{4k^2-k_z^2}}\sqrt{R^2+r_p^{\,2}-2\cdot R\cdot r_p\cos(\phi_p-\theta^*)}\right)}{\sqrt{R^2+r_p^{\,2}+\left(\frac{k_z}{\sqrt{4k^2-k_z^2}}\sqrt{R^2+r_p^{\,2}-2\cdot R\cdot r_p\cos(\phi_p-\theta^*)}\right)^2-2\cdot R\cdot r_p\cos(\phi_p-\theta^*)}}-k_z \tag{A2.5}$$

After algebraically manipulating (A2.5), the following expression is obtained:

$$\left.\frac{\partial\left(-2k\cdot L_p(\theta,z)+\varepsilon\theta+k_z z\right)}{\partial z}\right|_{(\theta=\theta^*,z=z^*)}=\frac{2k\left(\frac{k_z}{\sqrt{4k^2-k_z^2}}\sqrt{R^2+r_p^{\,2}-2\cdot R\cdot r_p\cos(\phi_p-\theta^*)}\right)}{\sqrt{\left(1+\frac{k_z^2}{4k^2-k_z^2}\right)\cdot\left(R^2+r_p^{\,2}-2\cdot R\cdot r_p\cos(\phi_p-\theta^*)\right)}}-k_z \tag{A2.6}$$

$$\left.\frac{\partial\left(-2k\cdot L_p(\theta,z)+\varepsilon\theta+k_z z\right)}{\partial z}\right|_{(\theta=\theta^*,z=z^*)}=\frac{2k\left(\frac{k_z}{\sqrt{4k^2-k_z^2}}\sqrt{R^2+r_p^{\,2}-2\cdot R\cdot r_p\cos(\phi_p-\theta^*)}\right)}{\sqrt{\frac{4k^2}{4k^2-k_z^2}\cdot\left(R^2+r_p^{\,2}-2\cdot R\cdot r_p\cos(\phi_p-\theta^*)\right)}}-k_z \tag{A2.7}$$

Finally, after further simplification, (A2.7) can be written as:

$$\left.\frac{\partial\left(-2k\cdot L_p(\theta,z)+\varepsilon\theta+k_z z\right)}{\partial z}\right|_{(\theta=\theta^*,z=z^*)}=\frac{2k\left(\frac{k_z}{\sqrt{4k^2-k_z^2}}\sqrt{R^2+r_p^{\,2}-2\cdot R\cdot r_p\cos(\phi_p-\theta^*)}\right)}{\frac{2k}{\sqrt{4k^2-k_z^2}}\cdot\sqrt{\left(R^2+r_p^{\,2}-2\cdot R\cdot r_p\cos(\phi_p-\theta^*)\right)}}-k_z \tag{A2.8}$$

$$\left.\frac{\partial\left(-2k\cdot L_p(\theta,z)+\varepsilon\theta+k_z z\right)}{\partial z}\right|_{(\theta=\theta^*,z=z^*)}=k_z-k_z=0 \tag{A2.9}$$

Next, the validity of (A2.2) will be evaluated using (θ^*, z^*). The IF of (3.5) along the θ scan trajectory is equal to:

$$\frac{\partial(-2k\cdot L_p(\theta,z)+\varepsilon\theta+k_z z)}{\partial\theta}=\frac{2k\cdot R\cdot r_p\cdot\sin(\phi_p-\theta)}{\sqrt{R^2+r_p{}^2+(z_p-z)^2-2\cdot R\cdot r_p\cos(\phi_p-\theta)}}-\varepsilon. \tag{A2.10}$$

During the initial stage in next mathematical analysis, the term $(\phi_p-\theta^*)$ would not be expanded in order to make the process easier to follow:

$$\left.\frac{\partial(-2k\cdot L_p(\theta,z)+\varepsilon\theta+k_z z)}{\partial\theta}\right|_{(\theta=\theta^*,z=z^*)}=\frac{2k\cdot R\cdot r_p\cdot\sin(\phi_p-\theta^*)}{\sqrt{R^2+r_p{}^2+\left(z_p-z_p-\frac{k_z}{\sqrt{4k^2-k_z^2}}\sqrt{R^2+r_p{}^2-2\cdot R\cdot r_p\cos(\phi_p-\theta^*)}\right)^2-2\cdot R\cdot r_p\cos(\phi_p-\theta^*)}}-\varepsilon \tag{A2.11}$$

$$\left.\frac{\partial(-2k\cdot L_p(\theta,z)+\varepsilon\theta+k_z z)}{\partial\theta}\right|_{(\theta=\theta^*,z=z^*)}=\frac{2k\cdot R\cdot r_p\cdot\sin(\phi_p-\theta^*)}{\sqrt{R^2+r_p{}^2+\left(\frac{k_z}{\sqrt{4k^2-k_z^2}}\sqrt{R^2+r_p{}^2-2\cdot R\cdot r_p\cos(\phi_p-\theta^*)}\right)^2-2\cdot R\cdot r_p\cos(\phi_p-\theta^*)}}-\varepsilon \tag{A2.12}$$

$$\left.\frac{\partial(-2k\cdot L_p(\theta,z)+\varepsilon\theta+k_z z)}{\partial\theta}\right|_{(\theta=\theta^*,z=z^*)}=\frac{2k\cdot R\cdot r_p\cdot\sin(\phi_p-\theta^*)}{\frac{2k}{\sqrt{4k^2-k_z^2}}\cdot\sqrt{(R^2+r_p{}^2-2\cdot R\cdot r_p\cos(\phi_p-\theta^*))}}-\varepsilon. \tag{A2.13}$$

By substituting $(\phi_p-\theta^*)=-\alpha^*-\beta^*+\pi$, and the α^* and β^* values given in (3.17) and (3.18), and applying basic trigonometric identities, the following expression follows:

$$\left.\frac{\partial\left(-2k\cdot L_p(\theta,z)+\varepsilon\theta+k_z z\right)}{\partial\theta}\right|_{(\theta=\theta^*,z=z^*)}=\frac{\left(\sin(\alpha^*)\cos(\beta^*)+\sin(\beta^*)\cos(\alpha^*)\right)}{\frac{1}{\sqrt{4k^2-k_z^2}}\cdot\sqrt{\left(R^2+r_p{}^2+2\cdot R\cdot r_p\left(\cos(\alpha^*)\cos(\beta^*)-\sin(\alpha^*)\sin(\beta^*)\right)\right)}}-\varepsilon \qquad \text{(A2.14)}$$

$$\left.\frac{\partial\left(-2k\cdot L_p(\theta,z)+\varepsilon\theta+k_z z\right)}{\partial\theta}\right|_{(\theta=\theta^*,z=z^*)}=$$

$$\frac{R\cdot r_p\cdot\left(\frac{\varepsilon\sqrt{\left(4k^2-k_z^2\right)R^2-\varepsilon^2}}{\left(4k^2-k_z^2\right)R\cdot r_p}+\frac{\varepsilon\sqrt{\left(4k^2-k_z^2\right)r_p^2-\varepsilon^2}}{\left(4k^2-k_z^2\right)R\cdot r_p}\right)}{\frac{1}{\sqrt{4k^2-k_z^2}}\cdot\sqrt{\left(R^2+r_p{}^2+2\cdot R\cdot r_p\left(\frac{\sqrt{\left(4k^2-k_z^2\right)R^2-\varepsilon^2}\sqrt{\left(4k^2-k_z^2\right)r_p^2-\varepsilon^2}}{\left(4k^2-k_z^2\right)R\cdot r_p}-\frac{\varepsilon^2}{\left(4k^2-k_z^2\right)R\cdot r_p}\right)\right)}}-\varepsilon \qquad \text{(A2.15)}$$

$$\left.\frac{\partial\left(-2k\cdot L_p(\theta,z)+\varepsilon\theta+k_z z\right)}{\partial\theta}\right|_{(\theta=\theta^*,z=z^*)}=\frac{\frac{\varepsilon\left(\sqrt{\left(4k^2-k_z^2\right)R^2-\varepsilon^2}+\sqrt{\left(4k^2-k_z^2\right)r_p^2-\varepsilon^2}\right)}{\left(4k^2-k_z^2\right)}}{\frac{1}{\sqrt{4k^2-k_z^2}}\cdot\sqrt{\left(\frac{\left(4k^2-k_z^2\right)\left(R^2+r_p{}^2\right)+2\left(\sqrt{\left(4k^2-k_z^2\right)R^2-\varepsilon^2}\sqrt{\left(4k^2-k_z^2\right)r_p^2-\varepsilon^2}-\varepsilon^2\right)}{\left(4k^2-k_z^2\right)}\right)}}-\varepsilon\ .$$

(A2.16)

In order to further simplify (A2.16), the radical term in the denominator will be factorized. The result is:

$$\left.\frac{\partial\left(-2k\cdot L_p(\theta,z)+\varepsilon\theta+k_z z\right)}{\partial\theta}\right|_{(\theta=\theta^*,z=z^*)}=\frac{\frac{\varepsilon\left(\sqrt{\left(4k^2-k_z^2\right)R^2-\varepsilon^2}+\sqrt{\left(4k^2-k_z^2\right)r_p^2-\varepsilon^2}\right)}{\left(4k^2-k_z^2\right)}}{\frac{1}{4k^2-k_z^2}\cdot\sqrt{\left(\sqrt{\left(4k^2-k_z^2\right)R^2-\varepsilon^2}+\sqrt{\left(4k^2-k_z^2\right)r_p^2-\varepsilon^2}\right)^2}}-\varepsilon \qquad \text{(A2.17)}$$

Finally, by further manipulating (A2.17), we obtain:

$$\left.\frac{\partial\left(-2k\cdot L_p(\theta,z)+\varepsilon\theta+k_z z\right)}{\partial\theta}\right|_{(\theta=\theta^*,z=z^*)}=\frac{\varepsilon\left(\sqrt{\left(4k^2-k_z^2\right)R^2-\varepsilon^2}+\sqrt{\left(4k^2-k_z^2\right)r_p^2-\varepsilon^2}\right)}{\left(\sqrt{\left(4k^2-k_z^2\right)R^2-\varepsilon^2}+\sqrt{\left(4k^2-k_z^2\right)r_p^2-\varepsilon^2}\right)}-\varepsilon \tag{A2.18}$$

$$\left.\frac{\partial\left(-2k\cdot L_p(\theta,z)+\varepsilon\theta+k_z z\right)}{\partial\theta}\right|_{(\theta=\theta^*,z=z^*)}=\varepsilon-\varepsilon=0 \quad . \tag{A2.19}$$

Therefore (θ^*,z^*) is a valid stationary point for the spf given in (3.4).

REFERENCES

[1] D. Daniels, *Ground Penetrating Radar*, IEE Press, London, UK, 2004.

[2] Langman and M. R. Inggs, "Pulse Versus Stepped Frequency Continuous Wave Modulation for Ground Penetrating Radar," *IEEE International Geoscience and Remote Sensing Symposium*, July 2001.

[3] R. Stolt, "Migration by Fourier Transform," *Geophysics*, vol. 43, pp. 23-48, 1978.

[4] Georgiana Daian, Alexander Taube, Amikam Birnboim, Mihai Daian and Yury Shramkov, "Modeling the Dielectric Properties of Wood," *Wood Science and Technology*, vol. 40, pp. 237–246, January 2006.

[5] L.M. Sheppard, "Not your Mother's Mammography [Breast Cancer Detection]," *IEEE Spectrum,* vol. 39, pp. 56-57, October 2002.

[6] N. Milisavljevic and A. G. Yarovoy, "An Effective Algorithm for SubsurfaceSAR Imaging," *IEEE International Symposium Antennas and PropagationSociety*, June 2002.

[7] D. Flores-Tapia and G. Thomas, "Breast Microwave Imaging and Focusing based on Range Migration Techniques," *16th Int. Zurich Symposium on Electromagnetic Compatibility, Topical Meeting on Biomedical EMC*, February 2005.

[8] M. Soumekh, *Synthetic Aperture Radar Signal Processing with MATLAB Algorithms*, Wiley-Interscience, New York City, New York, USA, 1999.

[9] E. Corral, *Real Time Imaging System for a Ground Penetrating Radar*, M. Sc. Thesis, Department of Electrical and Computer Engineering, The University of Manitoba, Canada, 2003.

[10] Milman, "SAR Imaging by ω-k Migration," *International Journal of Remote Sensing*, vol. 14, 1965-1979, October 1993.

[11] E. J. Bond, Xu Li, S. C. Hagness and B. D Van Veen, "Microwave Imaging via Space-Time Beamforming for Early Detection of Breast Cancer," *IEEE Transactions on Antennas and Propagation*, vol. 51, pp. 1690 – 1705, August 2003.

[12] E. C. Fear and M. A. Stuchly, "Microwave Detection of Breast Cancer," *IEEE Transactions on Microwave Theory and Techniques*, vol. 48, pp. 1854 – 1863, November 2000.

[13] D. Flores-Tapia, G. Thomas and S. Pistorius, "A Wavefront Reconstruction Method for 3D Cylindrical Subsurface Radar Imaging," *IEEE Transactions on Image Processing*, vol. 17, pp. 1908-1925, October 2008.

[14] P. Kosmas, C.M. Rappaport, "Time Reversal with the FDTD Method for Microwave Breast Cancer Detection," *IEEE Transactions on Microwave Theory and Techniques*, vol. 53, pp. 2317-2323, July 2005.

[15] R. Wu, K. Gu, J. Li, M. Bradley, J. Habersat and G. Maksymonko, "Propagation Velocity Uncertainty on GPR SAR Processing," *IEEE Transactions on Aerospace and Electronic Systems*, vol. 39, pp. 849 – 861, July 2003.

[16] E.C. Fear, S.C. Hagness, P.M. Meaney, M. Okoniewski, M.A. Stuchly, "Enhancing breast tumor detection with near-field imaging," *IEEE Microwave Magazine,* vol. 3, pp. 48-56, Mar 2002.

[17] J.M. Sill, E.C. Fear, "Tissue Sensing Adaptive Radar for Breast Cancer Detection - Experimental Investigation of Simple Tumor Models," *IEEE Transactions on Microwave Theory and Techniques,* vol. 53, pp. 3312-3319, November 2005.

[18] Xu Li and S. C. Hagness, "A Confocal Microwave Imaging Algorithm for Breast Cancer Detection", *IEEE Microwave and Wireless Components Letters*, vol. 11, pp. 130 – 132, March 2001.

[19] P. Kosmas, C.M. Rappaport, “Modeling with the FDTD Method for Microwave Breast Cancer Detection,” *IEEE Transactions on Microwave Theory and Techniques*, vol. 52, pp. 1890-1897, August 2004.

[20] M. Soumekh, “Reconnaissance with Ultra Wideband UHF Synthetic Aperture Radar,” *IEEE Signal Processing Magazine*, vol. 12, pp. 21-40, July 1995.

[21] M. Soumekh, *Fourier Array Imaging*, Prentice Hall, Englewood Cliffs, New Jersey, USA, 1994.

[22] M. Soumekh, “A System Model and Inversion for Synthetic Aperture Radar Imaging,” *IEEE Transactions in Image Processing*, vol. 1, pp. 64-76, January 1992.

[23] E. C. Fear, J. Sill, and M. A. Stuchly, “Experimental Feasibility Study of Confocal Microwave Imaging for Breast Tumor Detection,” *IEEE Transactions on Microwave Theory and Techniques*, vol. 51, pp. 887 – 892, March 2003.

[24] J. Goodman, *Introduction to Fourier Optics*, McGraw Hill, New York City, New York, USA, 1968.

[25] A. Papoulis, *Systems and Transforms with Applications in Optics*, McGraw-Hill,, New York City, New York, USA, 1968.

[26] J.M. Lopez-Sanchez, J. Fortuny-Guasch, "3D Radar Imaging using Range Migration Techniques," *IEEE Transactions on Antennas and Propagation*, vol. 48, pp. 728-737, May 2000.

[27] J.G. Proakis, D.G. Manolakis, *Digital Signal Processing*, Prentice-Hall, Upper Saddle River, New Jersey, USA, 1996.

[28] D. Flores-Tapia, G. Thomas, and S. Pistorius, "Wavefront Reconstruction of Breast Microwave Imagery Acquired Along Circular Scan Trajectories: A Study on Experimental Feasibility," *Progress in Electromagnetics Research Symposium*, March 2008.

[29] M. Soumekh, "Band-limited Interpolation from Unevenly Sampled Data," *IEEE Transactions on Acoustics, Speech and Signal Processing*, vol. 36, pp.110-122, January 1988.

[30] D. Flores-Tapia, G. Thomas, and S. Pistorius, "On the Quality of Breast Microwave Imagery Using Different Radiation Footprints," *18th International Conference on Applied Electromagnetics and Communications*, October 2005.

[31] D. R. Wehner, *High-Resolution Radar*, Artech House Inc., Norwood, Massachusetts, USA, 2001.

[32] D. Flores-Tapia, G. Thomas, A. Sabouni, S. Noghanian, and S. Pistorius, "Breast Tumor Microwave Simulator Based on a Radar Signal Model," *IEEE International Symposium on Signal Processing and Information Technology*, August 2006.

[33] D. Flores-Tapia, G. Thomas, and S. Pistorius, "Skin Surface Removal on Breast Microwave Imagery," *SPIE Symposium on Medical Imaging*, February 2006.

[34] S. Mallat, and S. Zhong, "Characterization of Signals from Multiscale Edges," *IEEE Transactions on Pattern Analysis and Machine Intelligence*, vol. 14, pp. 710–732, July 1992.

[35] J. M Sill and E. C. Fear, "Tissue Sensing Adaptive Radar for Breast Cancer Detection: Study of Immersion Liquids," *Electronics Letters*, vol. 41, pp. 113–115, February 2005.

[36] D. Flores-Tapia, G. Thomas and B. C. Flores, "Estimation of Medium Permittivity for Subsurface Radar Imaging Based on Conditional Entropy Metrics," *18th International Conference on Applied Electromagnetics and Communications*, Dubrovnik, Croatia, October 2005.

[37] J. Sok-Son, G. Thomas, and B. C. Flores, *Range-Doppler Radar Imaging and Motion Compensation*, Artech House Inc., Norwood, Massachusetts, USA, 2001.

[38] E.C. Fear, Xu Li, S.C. Hagness, M.A. Stuchly, "Confocal Microwave Imaging or Breast Cancer Detection: Localization of Tumors in Three Dimensions", *IEEE Transactions in Biomedical Engineering*, vol. 49, pp. 812-821, August 2002.

[39] E. C. Fear and M. Okoniewski, "Confocal Microwave Imaging for Breast Tumor Detection: Application to a Hemispherical Breast Model," *2002 IEEE MTT-S International Microwave Symposium Digest*, June 2002.